*Review*

# MXene/Ferrite Magnetic Nanocomposites for Electrochemical Supercapacitor Applications

Arun Thirumurugan [1,\*], Ananthakumar Ramadoss [2], Shanmuga Sundar Dhanabalan [3], Sathish-Kumar Kamaraj [4], Natarajan Chidhambaram [5], Suyambrakasam Gobalakrishnan [6], Carolina Venegas Abarzúa [1], Yerko Alejandro Reyes Caamaño [1], Rednam Udayabhaskar [7] and Mauricio J. Morel [7]

1 Sede Vallenar, Universidad de Atacama, Costanera #105, Vallenar 1612178, Chile
2 Advanced Research School for Technology & Product Simulation (ARSTPS), School for Advanced Research in Polymers (SARP), Central Institute of Petrochemicals Engineering & Technology (CIPET), T.V.K. Industrial Estate, Guindy, Chennai 600032, Tamil Nadu, India
3 Functional Materials and Microsystems Research Group, RMIT University, Melbourne, VIC 3000, Australia
4 Tecnológico Nacional de México, Instituto Tecnológico El Llano, El Llano 20330, Mexico
5 Department of Physics, Rajah Serfoji Government College (Autonomous), Bharathidasan University, Thanjavur 613005, Tamil Nadu, India
6 Department of Nanotechnology, Noorul Islam Centre for Higher Education, Deemed to be University, Kumaracoil 629180, Tamil Nadu, India
7 Instituto de Investigaciónes Científicasy Tecnológicas (IDICTEC), Universidad de Atacama, Copayapu 485, Copiapo 1531772, Chile
\* Correspondence: arun.thirumurugan@uda.cl or arunthiruvbm@gmail.com; Tel.: +56-971623332

**Abstract:** MXene has been identified as a new emerging material for various applications including energy storage, electronics, and bio-related due to its wider physicochemical characteristics. Further the formation of hybrid composites of MXene with other materials makes them interesting to utilize in multifunctional applications. The selection of magnetic nanomaterials for the formation of nanocomposite with MXene would be interesting for the utilization of magnetic characteristics along with MXene. However, the selection of the magnetic nanomaterials is important, as the magnetic characteristics of the ferrites vary with the stoichiometric composition of metal ions, particle shape and size. The selection of the electrolyte is also important for electrochemical energy storage applications, as the electrolyte could influence the electrochemical performance. Further, the external magnetic field also could influence the electrochemical performance. This review briefly discusses the synthesis method of MXene, and ferrite magnetic nanoparticles and their composite formation. We also discussed the recent progress made on the MXene/ferrite nanocomposite for potential applications in electrochemical supercapacitor applications. The possibility of magnetic field-assisted supercapacitor applications with electrolyte and electrode materials are discussed.

**Keywords:** MXene; ferrites; supercapacitor applications

## 1. Introduction

MXene, a class of 2D transition metal carbides/nitrides, has been identified as a new emerging material for various applications including energy storage, electronics, and bio-related due to its wider physical characteristics. Further, the formation of hybrid composites of MXene with other materials introduces interesting uses in multifunctional applications. MXene offers tremendous promise for energy storage applications, due to its lamellar construction, outstanding density, conductivity, configurable terminations, and ionic pseudocapacitance charge storage process [1–3]. A wide variety of MXenes are produced by diverse mixtures of transition metals, carbon and/or nitrogen, and diverse n layers; however, only a few have been generated and employed in energy storage applications thus far, with $Ti_3C_2Tx$ being the most investigated [4–9]. The possible MAX phase associated

with MXene, compositions, and structure of typical MXene and some of the experimentally prepared MXenes are shown in Figure 1. By removing the A layers from the MAX phase, MXenes are created. The compound is recognized as MXene due to its composition, which is $M_{n+1}AX_n$, where M is an initial transition metal, A is primarily an element from group IIIA or IVA (i.e., 13 or 14), X is C and/or N, and n is either 1, 2, or 3. The composition of the MAX phase and MXene compound, tuning of composition of MXene and the possible MXene could be understood from Figure 1a–c. MXenes represent a new large family that extends the world of 2D materials, and there has been an increase in interest in 2D materials other than graphene. Distinctive morphologies, strong electronic conductivities, and diverse chemistries, among other distinctive features of MXenes, have made them desirable in numerous applications, particularly for energy storage [10]. Due to its renowned etching processes and the extensive theoretical and experimental investigations on its physico-chemical and electrochemical characteristics, $Ti_3C_2T_x$, one prominent example among the MXene group, is a key interest of many. The electrochemical characteristics of MXene have been debated in recent years with some experimental evidence [3,6,11–13]. In aqueous electrolytes, hydrated cations are intercalated into MXene electrodes. Within the constrained potential window, the hydrated cations establish an electric double layer throughout the interlayer region to provide a standard capacitance. When nonaqueous electrolytes are utilized, the limited solvation shell must progressively breakdown due to the significant internal potential difference in the interlayer, even when solvated ions are diffused into the interlayer during the early phase of charging. Desolvated ions only intercalate when charged more, and a donor band is formed when the desolvated cations' atomic orbitals cross over with those of MXene. By the charge transition from the metal ions to MXene, the reduction of MXene caused by the donor band development results in an intercalation pseudocapacitance. The detailed charge storage mechanism was explored by a few recent studies [3,13–15]. Further the improvement in the charge storage capacity could be enhanced through the surface modification process [16].

Spinel ferrites are homogeneous substances that have the typical chemical form of $AB_2O_4$, where A and B are metallic ions that are located at 2 distinct crystallographic places, tetrahedral (A sites) and octahedral (B sites), respectively, with key elements of $Fe^{3+}$ in their structure. Three distinct spinel ferrite configurations, termed as normal, inverse, and mixed systems, are attainable for the composition of $MFe_2O_4$, based on the position of $M^{2+}$ and $Fe^{3+}$ location selection. $M^{2+}$ is distributed at the tetrahedral location and $Fe^{3+}$ at the octahedral location in a typical spinel configuration of ferrite. $Fe^{3+}$ is evenly located at both positions in an inverse spinel configuration, whereas $M^{2+}$ solely resides at the octahedral location. Both ions are indiscriminately located at the tetrahedral and octahedral positions in a mixed spinel configuration. $Fe_3O_4$ is considered an intriguing material for energy storage systems due to additional benefits such as high theoretical-specific capacitance (2299 F/g), a wide potential window (−1.2 to 0.25 V), abundance in nature, relative inexpensiveness, lesser toxicity, etc., [17]. The charge storage mechanism in various ferrites was thoroughly analyzed by various experimental methods in supercapacitor applications [17–20]. All these kinds of ferrite could be easily prepared by selecting suitable precursors for suitable experimental procedures.

The MXene/Ferrite composites have attracted much attention in various applications including batteries, electrochemical supercapacitors, photocatalytic degradation, electro-magnetic shield, and water purification methods [23–29]. The charge storing capacity of various MXenes and ferrites was not achieved towards its theoretical capacity. There are many ongoing investigations focused on improvement in the electrochemical performance of different MXenes, as well as on the various ferrites by adjusting the shape, size, and functional groups. The formation hybrid materials could be advantageous to achieve better outcomes from both materials due to the synergic effect.
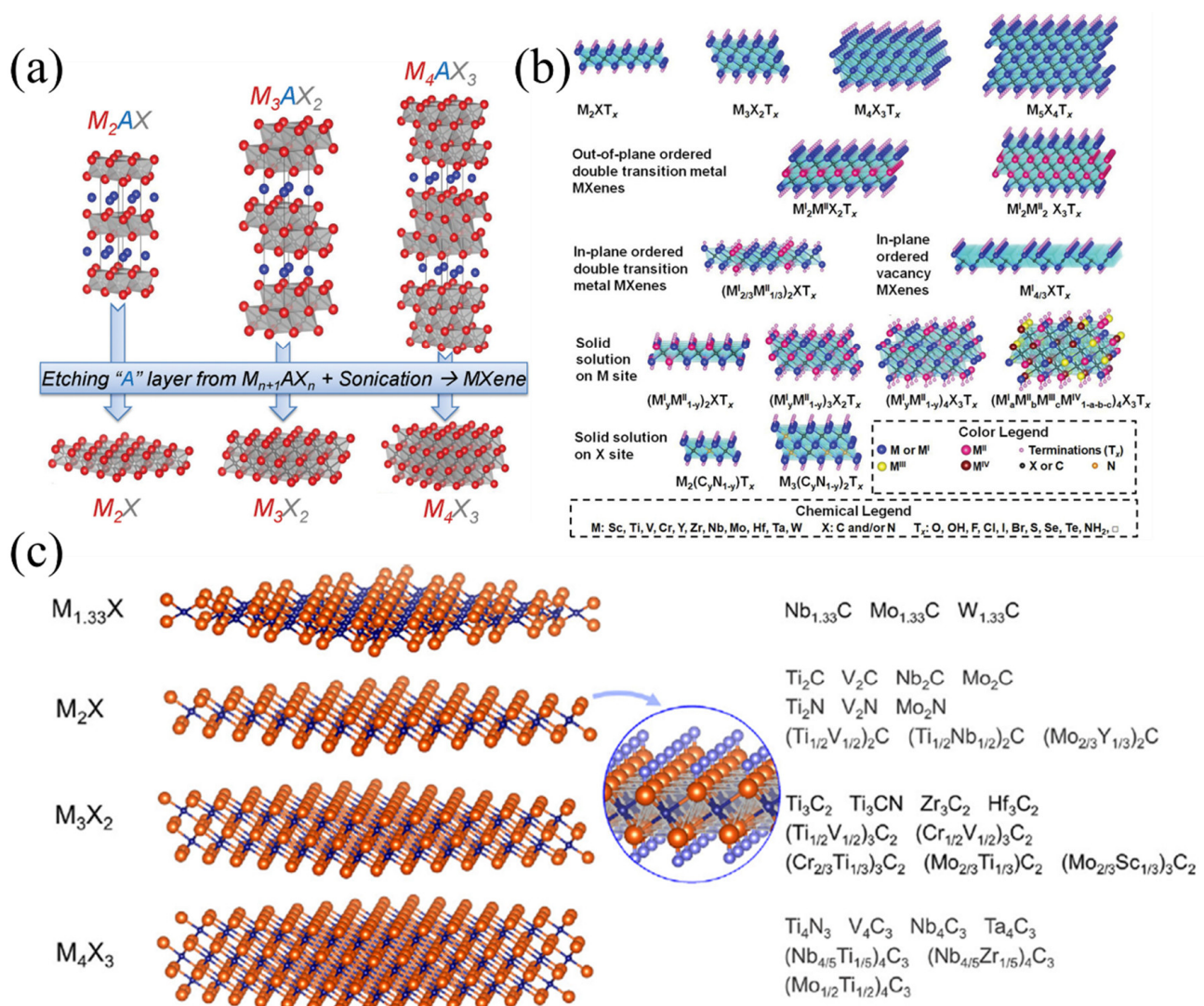
**Figure 1.** (**a**) MAX phase structures and their associated MXenes. Reproduced with permission from [5] Copyright (2013) John Wiley & Sons. (**b**) Usual MXene compositions and structures. Reproduced with permission from [21] Copyright (2021) John Wiley & Sons. (**c**) Experimentally discovered MXenes: structural and molecular formula. Reproduced with permission from [22] Copyright (2019) Elsevier.

The advantages of these magnetic nanocomposites over other available nanocomposites are its magnetic characteristics. These magnetic nanocomposites can be reused after the completion of any specific application. The collection processes of the magnetic nanocomposites are also easy to process with the external magnet because of the magnetic nature of the nanocomposites. Another advantage in this magnetic nanocomposite is the utilization of the eternal magnetic field during the application process. The presence of the external magnetic field with the magnetic nanocomposite definitely could influence the reaction mechanism, which could reflect in the efficiency of the nanocomposites in specific applications [30]. Green synthesis methods are also possible in the formation of these kinds of composites to obtain environmental sustainability. The effect of the external magnetic field on a few ferrites and non-magnetic materials has been studied. However, the optimization of external field strength for various magnetic and non-magnetic materials is much needed. The composite of MXene with ferrites requires attention as there are many opportunities to explore more nanocompositions.

## 2. Synthesis Methods

### 2.1. Preparation of MXene

MXene can be prepared through a top-down approach whereby the etching takes place using bottom-up methods, including chemical vapor deposition, pulsed laser deposition etc. [31–33]. However, the bottom-up approach has some limitations including the availability of precursors and desired size, which could be a challenging process through the chemical synthesis or chemical exfoliation process. The etching, delamination and filtration processes comprise the basic preparation process for scalable synthesis in the MAX phase [34]. Through a simple process that involves selectively eliminating the A component from the MAX form at room temperature, MXene synthesis can be performed [35]. In this procedure, the MAX phase substance is agitated in aqueous HF at a predetermined fraction for a predetermined amount of time, separated from the blends by centrifugation and/or filtering, and then washed by deionized water until the pH of the dispersion attains values between 4–6. The overall process is schematically shown in Figure 2.
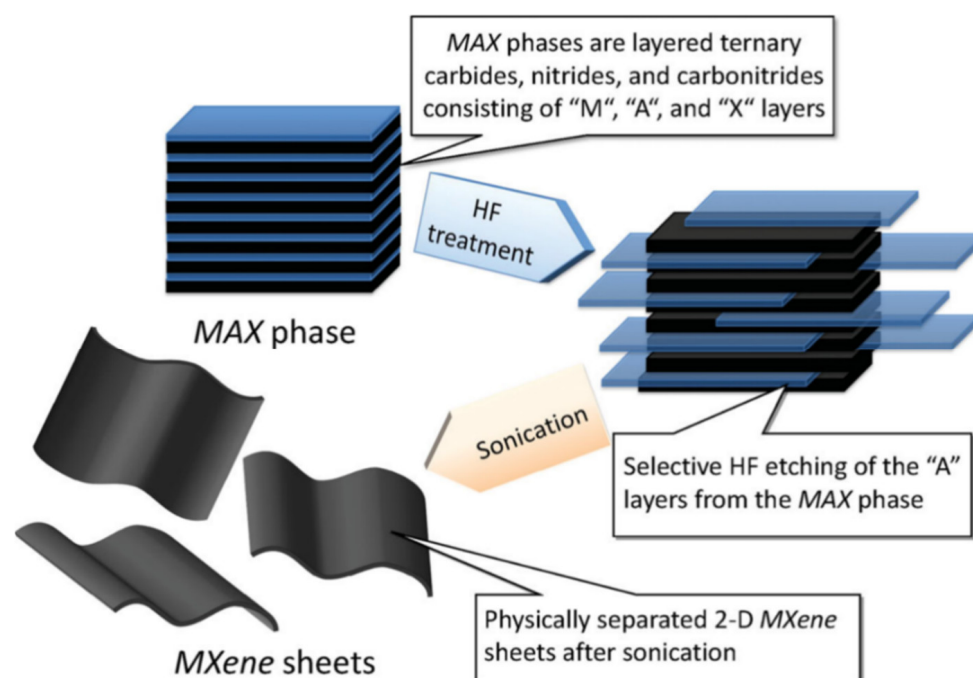


**Figure 2.** Schematic process of etching and exfoliation process of MXene from MAS phase. Reproduced with permission from [35] Copyright (2012) American Chemical Society.

The etching process can be done through hydrogen fluoride (HF), lithium fluoride (LiF)/HF, $NH_4HF_2$, molten salt etching, alkali treatment and the intercalation of additives such as hydrazine with N,N-dimethylformamide and dimethyl sulfoxide, and urea, tetrabutylammonium hydroxide, tetramethylammonium hydroxide, amine n-butylamine, and choline hydroxide [36–46]. As all these synthesis processes are progressing rigorously towards a better synthesis process, there are numerous opportunities to solve the present issues related to the scalable single-phase synthesis of MXene. Studies have etched $Ti_3C_2$ MXene and $Ti_2C$ MXene with LiF, potassium fluoride (KF), ammonium fluoride ($NH_4F$), and sodium fluoride (NaF) in hydrochloric acid (HCl), and then delaminated the resultant material with urea, dimethylsulfoxide, or ammonium hydroxide. Further optimizations were done with the time and temperature variation of the reaction process. The observed morphology of $Ti_3C_2$ and $Ti_2C$ for various conditions is shown in Figure 3.
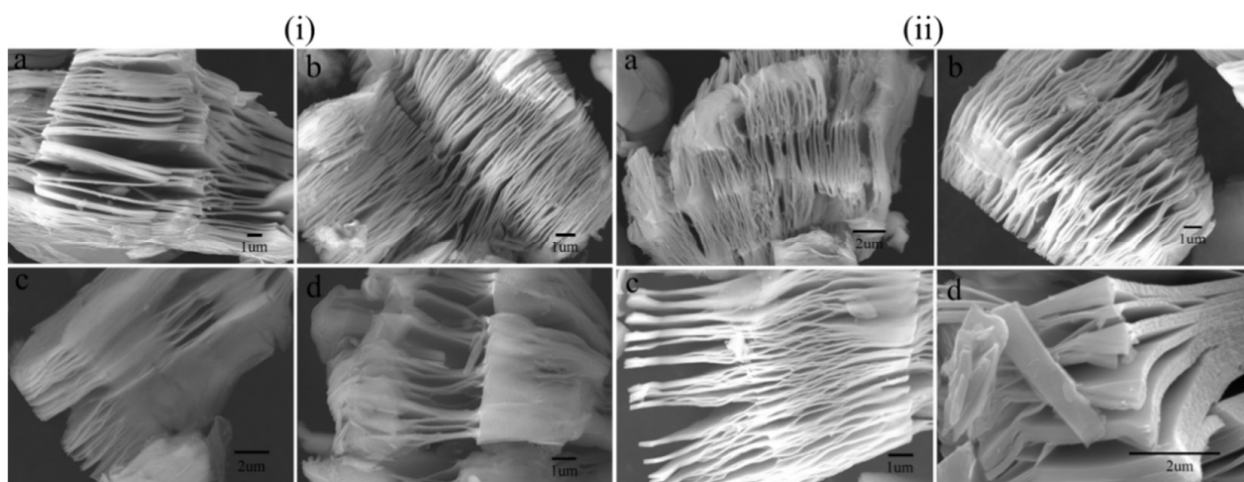
**Figure 3.** SEM micrograph of exfoliated MXene (**i**) ($Ti_3C_2$) with (**a**) LiF (**b**)NaF, (**c**) KF (**d**) $NH_4F$, in HCl, and (**ii**) ($Ti_2C$) with (**a**) LiF (**b**)NaF, (**c**) KF (**d**) NH4F, in HCl. Reproduced with permission from [47] Copyright (2017) Elsevier.

HF, which is extremely corrosive and detrimental to the functioning of Li-ion batteries and supercapacitors, is obviously used in the majority of the MXenes production processes. The preparation of a typical MXene—$Ti_3C_2T_x$ (T = OH, O) using an alkali-assisted hydrothermal technique has recently been reported for fluorine free synthesis of MXene [44]. This technique was modeled after a Bayer procedure that is frequently employed in the refinement of bauxite. Multilayer $Ti_3C_2T_x$ with a purity of 92 weight percent was produced by the complete procedure, which uses 27.5 M NaOH at 270 °C. Two stages make up the $OH^-$ attack on the Al layers in $Ti_3AlC_2$: oxidizing the Al to form Al (oxide) hydroxides and dissolving the Al (oxide) hydroxides in alkali as shown in Figure 4. $Ti_3AlC_2$'s exterior Al atoms are susceptible to oxidation and dissolve in NaOH as Al hydroxide is soluble in NaOH. These results in -OH or -O terminate the exposed Ti and Al atoms. The inner Al ions also oxidize if this etching procedure is allowed to continue. $Al(OH)_3$ and its AlO(OH) are unavoidably produced by the $OH^-$ attack, though. These insoluble compounds are prevented from easily interacting with OH to form soluble $Al(OH)_4^-$ due to the lattice confining provided by the Ti layers (Figure 4a). This kind of "jamming effect" must be removed because it prevents the synthesis of MXene. The Bayer procedure demonstrates that dissolving the aluminum (oxide) hydroxides requires considerable temperatures and larger alkali concentrations. This is ideal for getting rid of the obstructing Al compounds and will allow the entire selective etching process to move in the direction of formation of MXenes. The overall process is schematically shown in Figure 4. The SEM, TEM and HRTEM micrograph of prepared MXenes are shown in Figure 4b–d.

The stability of MXene is one of the important parameters to consider in any type of application [48,49]. In general, the MXene is easily oxidized or degraded from its original physicochemical characteristics. The oxidation of the $Ti_3C_2$ results in the formation of Ti-based oxide materials on the surface or anywhere in the MXene along with amorphous carbon. However, several procedures were demonstrated to control the oxidation or degradation process of MXenes [50]. A few of the processes include the synthesis of MXene with fewer defects, surface modification of MXene with organic ligands or any other suitable surface modifier, dispersions of MXenes in organic solutions, and the storing of MXene in solution, which is stored inside the inert gas-filled container [49,51]. If the MXene hybrids with polymeric materials or any other stable materials are required in particular applications, then the degradation of the stability and electronic conductivity of MXene could be reduced due to the polymeric or any other stable materials in hybrids [52].
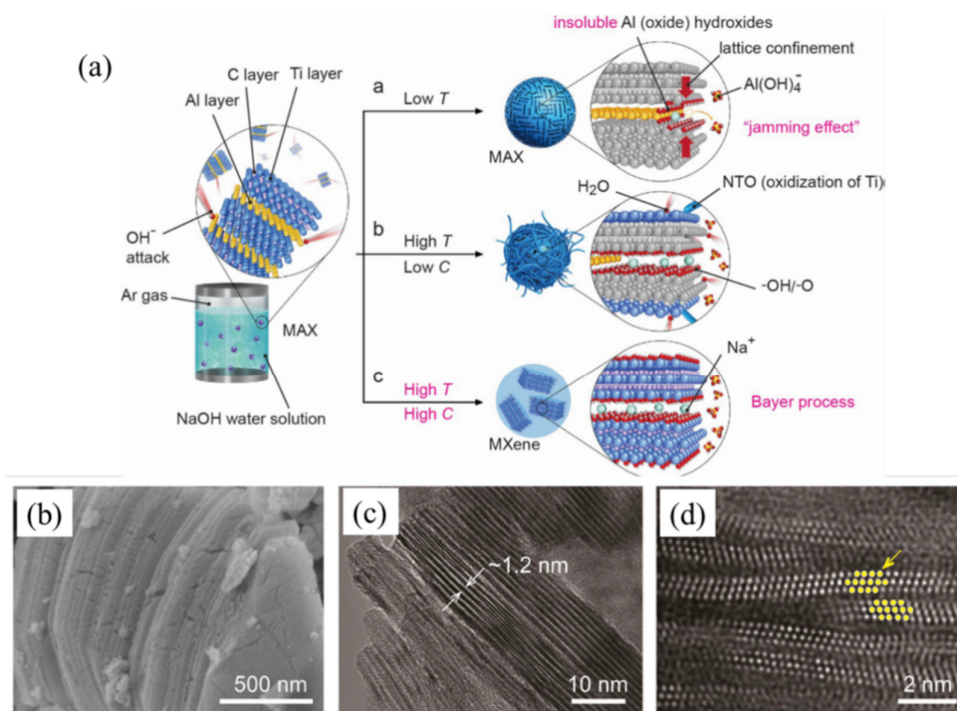
**Figure 4.** Diagram illustrating the interaction between a NaOH solution and $Ti_3AlC_2$ under various circumstances. ((**a**) At low temperatures, Al (oxide) hydroxides obstruct the extraction of Al. (**b**) In the presence of high temperatures and low NaOH conc, certain Al (oxide) hydroxides dissolve in NaOH. (**c**) Based on the Bayer mechanism, dissolving the Al (oxide) hydroxides in NaOH is aided by high temperatures and higher concentrations of NaOH), (**b–d**) SEM, TEM, and HRTEM micrograph of prepared MXene. Reproduced (modified) with permission from [44] Copyright (2018) John Wiley & Sons.

## 2.2. Synthesis of Ferrites

Numerous methods are available for the synthesis of various ferrites including co-precipitation, sol-gel, hydrothermal, solvothermal, the polyol process, and the chemical oxidation process [53–59]. However, the selection of the synthesis process is important to achieve the required shape and size of the desired ferrite. Chemical methods are preferred for the preparation of various ferrites due to the opportunity to tune the ferrite particle shape and size by modifying the experimental parameters including precursors, additives, reaction time, reaction temperature, and post-thermal treatment [60,61]. The co-precipitation method is a very common chemical method used to synthesize all kinds of ferrites. The co-precipitation method is a simple reaction process, and it can be completed within one hour depending on the ferrite stoichiometry.

The basic reaction mechanism for the formation of ferrites through the co-precipitation process is,

$$M^{2+} + M^{3+} + NaOH \ \rightarrow MFe_2O_4 + NaCl + H_2O \tag{1}$$
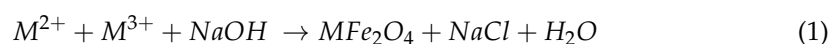
The divalent metal ions can be varied to form various forms of ferrites and doping of other metal ions, also a simple process in this reaction. Mono-sized ferrite particle formation is possible with optimized experimental parameters.

The chemical oxidation process is also a widely used chemical synthesis process for the formation of ferrites with larger size, and this method could be used to prepare the ferrites with a range of particle sizes. However, the formation of mono sized particles is challenging, and a wide range of particle size distribution is usually observed. The ferrite particle size can be tuned by varying the oxidant, precipitant and also by introducing the nucleating agent.

The general reaction process may be defined as,

$$M^{2+} + KNO_3 + NaOH \rightarrow MFe_2O_4 + KNO_2 + NaCl + H_2O \tag{2}$$
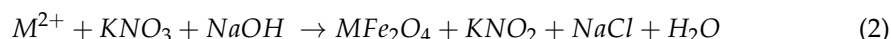
Several other methods were utilized for the development of various ferrites with tunable size, variable morphology by varying the experimental parameters, addition to the surfactant and doping process. Through the thermal decomposition process with the help of oleic acid (OA) and oleylamine (OAm), monodisperse magnetic Mn-Zn ferrite with a variety of morphologies from nanocrystals to clusters such as spherical, cubical and starlike nanocrystal have been effectively produced [62]. The reaction temperature and aging period affect whether nanocrystals will form. The fluctuation of the monomer fraction in the traditional La Mer model serves to assess the crystal nucleation/growth process in synthesis. For samples taken from all synthesis below 260 °C, no substance is seen. When the monomer is consistently utilized, irregular "crystal nuclei" (2–3 nm) are created at 260 °C, as shown in Figure 5A. At a later temperature of 260–300 °C, the first smaller-sized spheroidal nanocrystals are formed. When the aging period is increased from 20 to 40 min at 300 °C, a large number of uniform spherical nanocrystals in a closed packed array are generated. Small quasi-spherical shapes are initially produced in cubical and starlike morphology formation at the earlier temperatures (260–280 °C), as observed in Figure 5B and C. The result is mostly spherical with a tiny number of quasi-cubical shapes at the reaction's initial stage at 300 °C. Most of the nanocrystals remain growing as the aging duration at 300 °C is increased from 20 to 40 min, generating uniform cubical morphology with changes in size as shown in Figure 5B or continuing to form the eight corners of the half-formed precursors to create starlike nanocrystals as observed in Figure 5C. By altering the OA/OAm ratios, it is possible to successfully witness the uninterrupted shape transformation of nanocrystals from their initial sphericity, cubicity, to their final starriness, as schematically shown in Figure 5D.
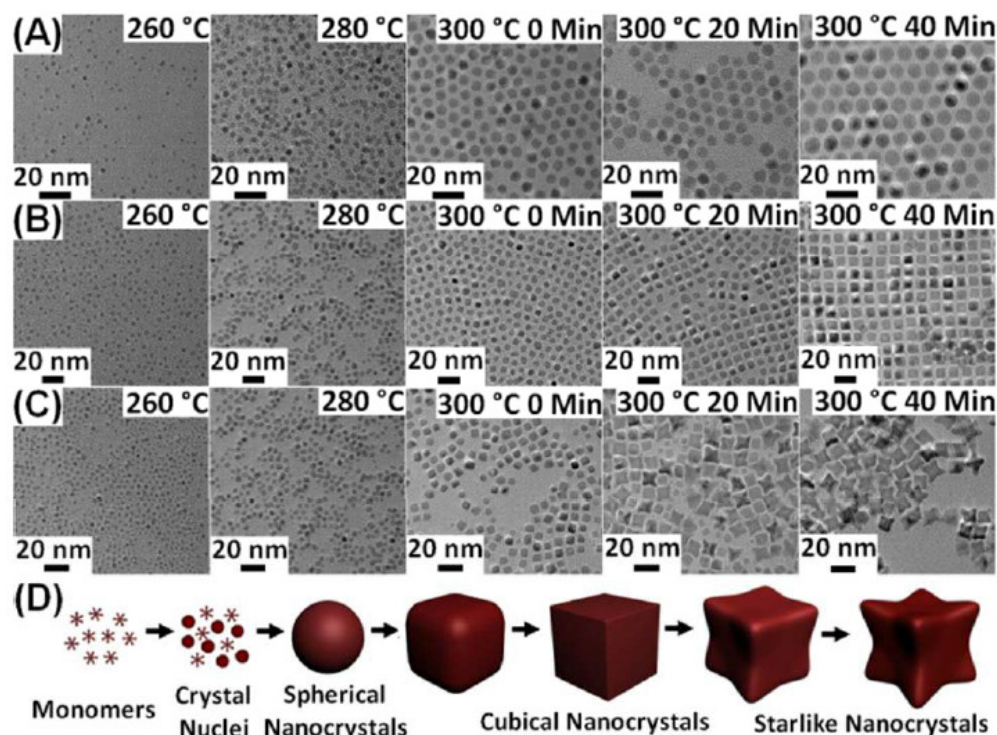


**Figure 5.** TEM micrograph of Mn-Zn ferrite nanocrystals collected from the reaction mixture at 260 °C, 280 °C, and 300 °C following aging for 0, 20, and 40 min. (**A**) spherical (**B**) cubical, and (**C**) starlike. (**D**) Evolution of the shape of starlike nanocrystals shown schematically. Reproduced with permission from [62] Copyright (2013) American Chemical Society.

Using a quick and affordable thermal decomposition approach, it was possible to successfully produce spherical, cubical, and hexagonal shaped Co-ferrite nanoparticles [63]. The TEM micrograph and particle size distribution of the developed cubical, spherical, and hexagonal shaped particles are shown in Figure 6. The optical band gaps, which vary according to the shape of the particles, were set between 1.41 and 1.32 eV. At 10 K and room temperature, respectively, hexagonal nanoparticles showed a superior coercivity of 17,845.8 and 1577.76 Oe than spherical and cubical shaped particles. Because hexagonal-shaped Co-ferrite has an extraordinary surface-to-volume ratio and supplementary structural facets, the coercivity can be altered. Due to the morphology-dependent cation allocation, different shaped particles have adjustable saturation magnetization, which is important for certain room temperature magnetic applications. The observed magnetic characteristics along with the calculated magnetic anisotropy values are listed in Table 1.
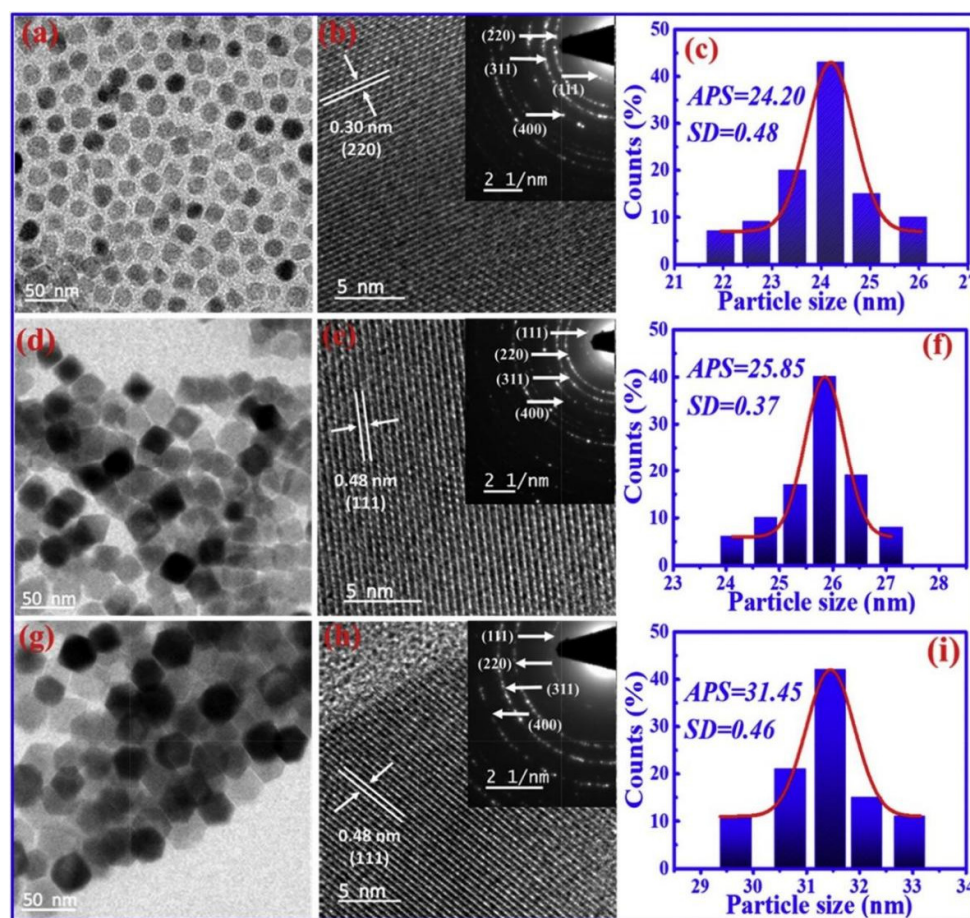


**Figure 6.** TEM, HRTEM micrograph and size distribution of (**a–c**) sphere-CoFe$_2$O$_4$ (**d–f**) cubic-CoFe$_2$O, and (**g–i**) hexagonal-CoFe$_2$O. Reproduced with permission from [63] Copyright (2019) Elsevier.

Without the use of a surfactant, a single moderate hydrothermal technique at 160 °C was used to synthesize Ni-ferrite with the morphologies of spheres, rods, and nano-octahedrons [64]. When the pH level was 7, nano-spheres with sizes of 10–25 nm were produced. At a pH level of 12, nano-rods with a length of around 1 m and width of 50–60 nm were generated. With a pH of 13, the sample's octahedral shape was discovered. Each side is approximately 150 nm long. Clearly, the Ni-ferrite nano-octahedrons' surface contains a few barely detectable nanoparticles. The schematic process for the formation mechanism of various shapes is shown in Figure 7. The saturation magnetization of nanooctahedrons and nanorods was measured as 55 and 40 emu/g. The spherical shaped particles did not show any saturation magnetization as the particle sizes are in the superparamagnetic regime.

This synthesis strategies could be adopted for the preparation of ferrite nanoparticles with different morphology where it may be required for the specific applications.

**Table 1.** Saturation magnetization, coercivity and K1 values of spherical, cubical and hexagonal shaped Co-ferrites [63].

| Temp | Spherical Co-Ferrite | | | Cubical Co-Ferrite | | | Hexagonal Co-Ferrite | | |
|---|---|---|---|---|---|---|---|---|---|
| | Ms (emu/g) | Hc (kOe) | K1 ($10^6$) | Ms (emu/g) | Hc (kOe) | K1 ($10^6$) | Ms (emu/g) | Hc (kOe) | K1 ($10^6$) |
| 10 | 81.11 | 17.31 | 3.11 | 83.21 | 17.05 | 2.91 | 86.11 | 17.85 | 3.38 |
| 50 | 79.46 | 13.62 | 2.57 | 81.14 | 12.75 | 2.43 | 84.63 | 14.09 | 2.78 |
| 100 | 76.94 | 10.36 | 2.31 | 78.18 | 9.48 | 2.11 | 82.74 | 11.38 | 2.44 |
| 150 | 75.08 | 6.64 | 1.89 | 77.24 | 6.35 | 1.78 | 80.73 | 6.81 | 2.24 |
| 200 | 73.55 | 4.47 | 1.48 | 74.72 | 3.89 | 1.34 | 78.48 | 4.67 | 1.75 |
| 250 | 72.9 | 3.02 | 1.21 | 73.14 | 2.83 | 1.23 | 76.15 | 3.18 | 1.42 |
| 300 | 70.68 | 1.39 | 0.98 | 71.74 | 1.09 | 0.89 | 75.32 | 1.58 | 1.11 |
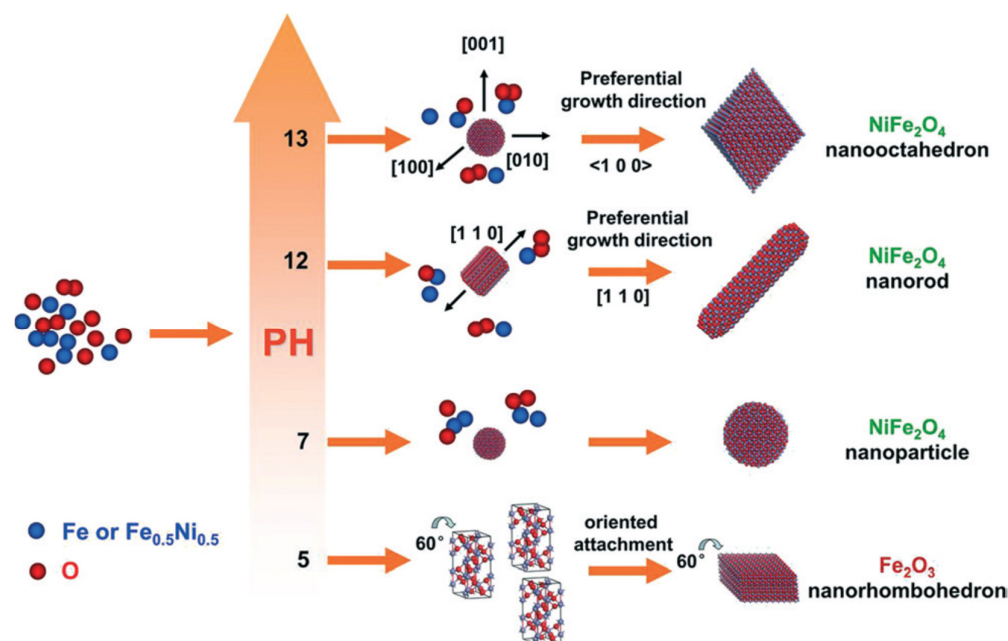


**Figure 7.** Schematic diagram for the different morphology formation processes of $\alpha$-Fe$_2$O$_3$ and Ni-ferrite. Reproduced with permission from [64] Copyright (2015) Royal Society of Chemistry.

Doping of metal ion into ferrite also could be used to alter the size and shape of the ferrite [65–70]. It is also noted that the particle size and shape influences the magnetic characteristics of the particle [71–74]. For the preparation of mixed ferrite, the divalent and trivalent metal ions can be introduced and adjusted for the complete phase formation with required cation distribution [75,76]. Similarly, other chemical methods such as the sonochemical process, solid state reaction, and auto-combustion method also could be adopted for the synthesis of various ferrite magnetic nanoparticles with the required shape and size [77–80].

## 2.3. MXene/Ferrite Composite Formation

The formation of composite is important as the application may require a synergic effect from hybrid materials. It is advantageous for the MXene to not have any nanomaterials between the layers to avoid the restacking. If the nanocomposite formation process is not

completely done, then there is a chance of the formation of two different materials without any physical or chemical attachment. To achieve the complete formation of composites of ferrites and MXenes, first the MXene should be covered with the ferric, ferrous, or any other metal ions before the formation of ferrites. The further addition of oxidant or reducing agent, depending on the experimental methods, could form the ferrites physically, chemically or physic-chemically attached on the surface of MXenes. Any of the above discussed chemical synthesis processes could be adopted for the formation of MXene composites with MXene. Further, the addition of any other attractive materials such as carbon-based materials is also possible for the formation of ternary composites with MXene.

The attachment of ferrites on MXene is important to be confirmed from any characterization techniques. The presence of ferrites on MXene could be evidenced from X-ray diffraction studies. But the manner of ferrite formation on the MXene could be evidenced through any microscopic methods. The fraction of ferrites in the MXene composites could be estimated from the magnetic hysteresis measurement, by estimating the saturation magnetization of bare ferrite and MXene/ferrite composites. The vibration modes can be analyzed through Fourier transform infrared spectroscopy and Raman spectroscopy methods. Further, the evidence of the metallic state of the metal ions present in the MXene composites could be analyzed from the X-ray photoelectron spectroscopy method. The specific surface area, pore size, and volume could be measured from the BET surface area measurement techniques. If we have strong evidence for the physicochemical characteristics of the MXene/ferrite, then the nanocomposite could be utilized for electro chemical energy storage applications.

Solvothermal synthesis was adopted for the synthesis of MXene/$Fe_3O_4$ nanocomposite with uniform distribution of $Fe_3O_4$ on the exterior and between the interlayers of MXene [81]. The simple schematic synthesis process was showed in Figure 8a. The particle sizes with 50–100 nm were observed for the $Fe_3O_4$ nanoparticles on the surface of MXenes in the MXene/$Fe_3O_4$ nanocomposites. Similarly, ultrasonic treatment is used to synthesize the MXene/$Fe_3O_4$ nanocomposite for the potential applications as additive sulfur cathode in the lithium−sulfur battery [29]. The schematic synthesis process for the $Fe_3O_4$ distributed on MXene nanocomposite formation is shown in Figure 8. The even distributions of $Fe_3O_4$ on the lamellar structure of Mxene were achieved and the improvement in the battery performance was evidenced.
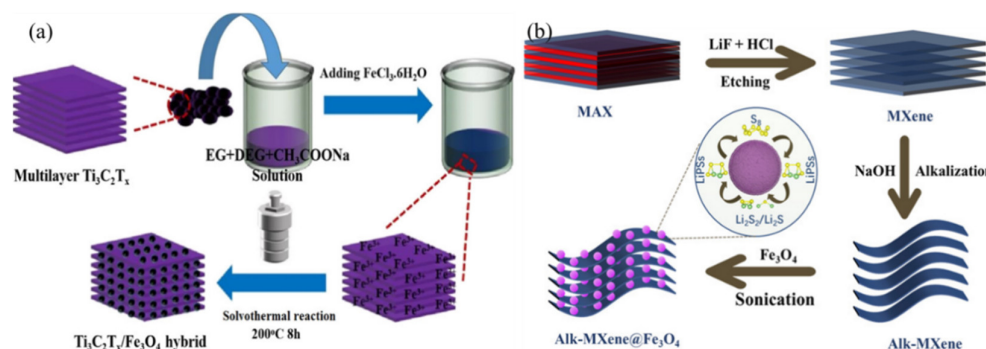


**Figure 8.** (**a**) Schematic synthesis process of Mxene/$Fe_3O_4$ nanocomposite through Solvothermal process. Reproduced with permission from [81]. (**b**) Schematic synthesis process of Alk-MXene composites with $Fe_3O_4$ through ultrasonic treatment. Reproduced with permission from [29] copyright (2022) John Wiley and Sons.

The successful nanocomposite formation was achieved by Xiaojun Yang et al. [27] with MXene and $Fe_3O_4$ through the hydrothermal, chemical etching, and vacuum filtration technique. The MXene nanosheets with the thickness of around 1 nm were decorated with the spherical nanoparticles of $Fe_3O_4$ with a size of a few dozen nanometers. The thin layer structure of MXene and the attachment of spherical $Fe_3O_4$ nanoparticles on the MXene layers were clearly evidenced from the TEM micrograph as shown in Figure 9.
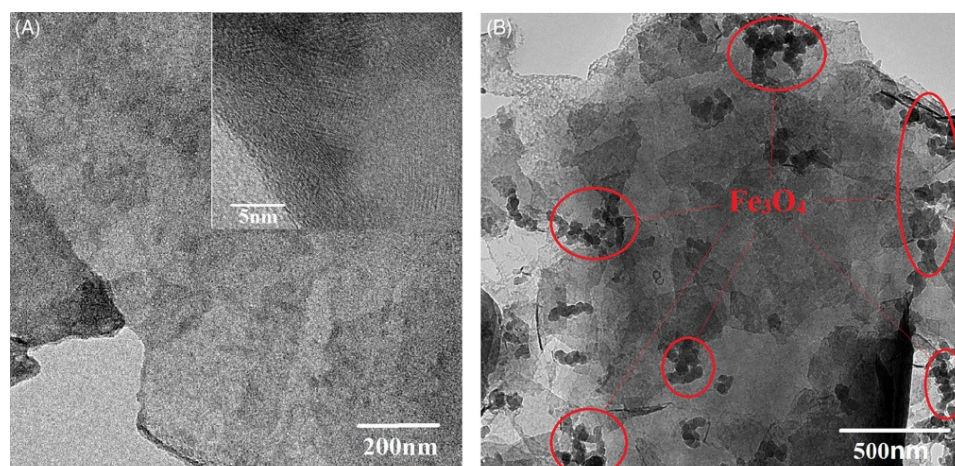
**Figure 9.** TEM micrographs of (**A**) MXene and (**B**) MXene/Fe$_3$O$_4$ nanocomposite. Reproduced with permission from [27] Copyright (2022) John Wiley and Sons.

Various forms of ferrites with MXene along with other materials have been developed and their physicochemical characteristics studied for various applications. Table 2 summarizes a few available combinations of MXene nanocomposites and their applications.

**Table 2.** MXene composites and their applications.

| S. No | Composites | Synthesis Method | Applications | Ref. |
|---|---|---|---|---|
| 1 | MXene/NiFe$_2$O$_4$ | In situ chemical co-precipitation method | microwave absorption | [82] |
| 2 | MXene/NiFe$_2$O$_4$ | ultrasonication | wastewater treatment and antibacterial activity | [83] |
| 3 | MXene/NiFe$_2$O$_4$ | one-step hydrothermal method | microwave absorption | [84] |
| 4 | MXene/Ni$_{0.5}$Zn$_{0.5}$Fe$_2$O$_4$ | co-precipitation process | electromagnetic wave absorption | [85] |
| 5 | MXene/CoFe$_2$O$_4$ | In situ solvothermal process | microwave absorption | [86] |
| 6 | MXene/CoFe$_2$O$_4$ | liquid self-assembly method | catalytic degradation of Naproxen | [87] |
| 7 | MXene/CoFe$_2$O$_4$ | hydrothermal synthesis | electromagnetic wave absorbing | [88] |
| 8 | MXene/CuFe$_2$O$_4$ | sol-gel/sonication | photocatalytic and antibacterial | [89] |
| 9 | MXene/La and Mn-co-doped Bismuth Ferrite | double-solvent sol–gel method | photocatalytic degradation of congo red dye | [90] |
| 10 | MXene/Fe$_3$O$_4$-myristicacid | in situ chemical synthesis strategy/physical vacuum infiltration | photothermal conversion | [91] |
| 11 | MXene/CoFe$_2$O$_4$ | sonication | supercapacitor | [24] |
| 12 | MXene/Fe$_3$O$_4$/RGO | modified chemical oxidation process | supercapacitor | [92] |
| 13 | MXene/Fe$_3$O$_4$/MXene | laser crystallization strategy | flexible supercapacitor | [93] |
| 14 | MXene/Co$_{0.7}$Zn$_{0.3}$Fe$_2$O$_4$/MWCNT | solvothermal process | electromagnetic absorption | [23] |
| 15 | MXene/Ni$_{0.6}$Zn$_{0.4}$Fe$_2$O$_4$ | In situ hydrothermal method | electromagnetic wave absorption | [94] |

**Table 2.** *Cont.*

| S. No | Composites | Synthesis Method | Applications | Ref. |
|-------|-----------|------------------|--------------|------|
| 16 | MXene/NiZn Ferrite | co-precipitation hydrothermal method | electromagnetic devices applications | [95] |
| 17 | MXene/Co-doped NiZn ferrite/polyaniline | exfoliation, hydrothermal process, and modified interfacial polymerization | electromagnetic wave absorption | [96] |
| 18 | MXene/$Fe_3O_4$/PANI | vacuum-assisted filtration | electromagnetic interference shielding | [97] |
| 19 | MXene/$Fe_3O_4$@PANI | co-precipitation and in-situ polymerization | wide-band electromagnetic absorber | [98] |
| 20 | MXene/$Fe_3O_4$/Au/PDA | hydrothermal/freeze dry | photo-thermal-magnetolytic coupling antibacterial | [99] |
| 21 | MXene/$Fe_3O_4$ | hydrothermal reaction | water splitting | [100] |
| 22 | MXene/Bismuth Ferrite | double-solvent solvothermal method | degradation of organic dyes and colorless pollutants | [101] |
| 23 | MXene/$Fe_3O_4$/C | microwave-assisted reaction, thermal treatment and sonication | electromagnetic absorption | [102] |
| 24 | MXene/$Ba_3Co_2Fe_{24}O_{41}$/Polyvinyl Butyral | tape-casting process | electromagnetic wave absorption | [103] |
| 25 | MXene/$Fe_3O_4$/$TiO_2$ | in situ oxidation | phosphoproteomics research | [104] |
| 26 | MXene/$Fe_3O_4$/MWCNTs | solvothermal and vacuum-assisted filtration method | electromagnetic interference shielding | [105] |
| 27 | RGO/MXene/$Fe_3O_4$ | ultrasonic spray technology | microwave absorbents | [106] |
| 28 | $Fe_3O_4$/MXene/polyurethane | – | stretchable electromagnetic shielding | [107] |
| 29 | MXene/$Fe_3O_4$/polyimide | In situ polymerization, electrospinning technology and vacuum-assisted filtration | electromagnetic interference shielding, electrothermal and photothermal conversion | [108] |
| 30 | MXene/$Fe_3O_4$ | thermal treatment | heterogeneous Fenton reaction catalyst towards MB, MO, RB and CR | [109] |
| 31 | MXene/$Fe_3O_4$ | chemical and filtration | removal of cationic dyes from aqueous media | [110] |
| 32 | MXene/$Fe_3O_4$ | ultrasonication | Li-ion batteries | [111] |
| 33 | MXene/$Fe_3O_4$ | hydrothermal and vacuum filtration process | heavy metal ions removal from wastewater | [27] |
| 34 | MXene/$Fe_3O_4$ | freeze-drying/freeze drying | Li-ion batteries | [112] |
| 35 | MXene/$Fe_3O_4$ | thermal decomposition process | microwave absorbing | [113] |
| 36 | MXene/$Fe_3O_4$ | biomimetic strategy-polymerization/sonication | photocatalytic degradation dyes | [114] |
| 37 | MXene/$Fe_3O_4$ | chemical hydrothermal reaction | microwave absorption | [115] |
| 38 | MXene/$Fe_3O_4$ | self-assembly approach | lithium-ion storage | [116] |
| 39 | MXene/$Fe_3O_4$ | solvothermal method | microwave absorbers | [81] |
| 40 | MXene/$Fe_3O_4$ | etching, sonication, self-assembly | nonlinear optics | [117] |

**Table 2.** *Cont.*

| S. No | Composites | Synthesis Method | Applications | Ref. |
|---|---|---|---|---|
| 41 | MXene/Fe$_3$O$_4$ | hydrothermal reaction method | microwave absorption | [118] |
| 42 | MXene/C/Fe$_3$O$_4$ | facile chemical process | Li-ion batteries | [119] |
| 43 | MXene/Fe$_3$O$_4$ | solvothermal process | microwave absorption | [120] |
| 44 | MXene/Fe$_3$O$_4$ | chemical and sonication | lightweight electromagnetic absorbers | [121] |
| 45 | MXene/Fe$_3$O$_4$ | in situ growth method | Li-ion storage | [122] |
| 46 | MXene/carbon coated Fe$_3$O$_4$ | – | Li-ion storage | [123] |
| 47 | waterborne polyurethane/MXene/NiFe$_2$O$_4$ | freeze-drying method | electromagnetic interference shielding | [124] |
| 48 | Fe$_3$O$_4$/MXene/carbon nanofibers | – | Li-ion batteries | [125] |
| 49 | Alk-MXene/Fe$_3$O$_4$ | ultrasonic treatment | lithium−sulfur batteries | [29] |
| 50 | MXene/Fe$_3$O$_4$-COOH | rapid gelation method | human motion monitoring | [126] |
| 51 | MXene/Fe$_3$O$_4$/3,4-dihydroxyphenylacetic acid (DOPAC)-epoxidized natural rubber (ENR) elastomers | – | flexible electromagnetic interference shielding | [127] |
| 52 | MXene/NiFe$_2$O$_4$/Carbon Felt | facile dip-and-dry and hydrothermal methods | microbial fuel cell | [128] |
| 53 | MXene/PPy/β$_2$-SiW$_{11}$Co/Fe$_3$O$_4$ | etching/sonication | electromagnetic wave absorption | [129] |
| 54 | Fe$_3$O$_4$-MXene-Carbon Nanotube | chemical precipitation method | supercapacitor | [130] |
| 55 | rGO/MXene (Nb$_2$CT$_x$)/Fe$_3$O$_4$ | hydrothermal treatment and self-assembly | absorption of electromagnetic wave | [131] |

From Table 2, it is clearly understood that there is much information available on the preparation of MXene/ferrites, which were utilized for the photocatalytic degradation of dyes, water purification and electromagnetic wave absorption. Few reports are available for the application of MXene/ferrites in batteries and fuel cells. However, very limited reports are available on the electrochemical super capacitive characteristics of MXene/ferrites nanocomposites. So, it is important to study the physicochemical and electrochemical characteristics of various MXene/ferrite nanocomposites to be utilized in next generation energy storage systems.

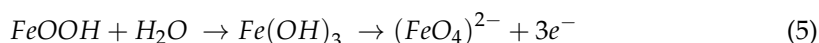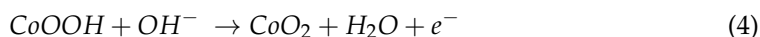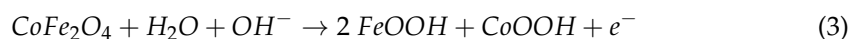**3. MXene/Ferrite Electrode for Supercapacitor Applications**

The utilization of multivalence metal ions in the mixed ferrite could be beneficial for the charge transfer process during electrochemical reactions. In this regard, Co-ferrite (CoFe$_2$O$_4$) has been attempted for the formation of nanocomposites with MXene due to the extraordinary theoretical specific capacitance, mixed valence, and chemical stability [24]. Co-ferrite is an established example of an inverse spinel in which Fe$^{3+}$ ions coexist with Co$^{2+}$ ions at tetrahedral regions and Fe$^{3+}$ ions at octahedral regions, resulting in enhanced redox activity and effective charge storage. The main issue with the Co-ferrite in supercapacitor applications is its low electronic conductivity. However, this could be solved by forming hybrid composites with other materials that have excellent electronic conductivity. The addition of Co-ferrite would be advantageous in MXene/Co-ferrite nanocomposites, as the Co-ferrite could be used to avoid the restacking of MXene layers. Co-precipitation with wet chemical etching processes were utilized for the formation of Co-ferrite and MXene. The MXene/Co-ferrite composite formation was achieved through the ultra-sonication process for one hour and dried at 80 °C in vacuum. The single phase of Co-Ferrite was evidenced for bare Co-ferrite nanoparticles as well as for the MXene/Co-ferrite

nanocomposite, and the observed XRD pattern of bare Co-ferrite and MXene/Co-ferrite are shown in Figure 10i(a,b). The characteristics reflections of MXene were not witnessed in the XRD pattern of MXene/Co-ferrite nanocomposite. However, the presence of MXene in the MXene/Co-ferrite nanocomposite was discussed through the observation if peak broadening occurs, variation in the lattice parameters and shift in the characteristic peak is observed. The observed peak broadening and peak shift are shown in Figure 10i(c,d). The SEM micrograph confirms the Co-ferrite nanoparticles sizes ranging from 70–90 nm and the layers construction of MXene as shown in Figure 10ii(a–c). The uniform dispersion of Co-ferrite over the MXene layered structure was evidenced from the SEM micrograph as shown in Figure 10ii(d). It is also noted that the Co-ferrite nanoparticles were also incorporated between MXene layers, which would be advantageous for the supercapacitor applications.
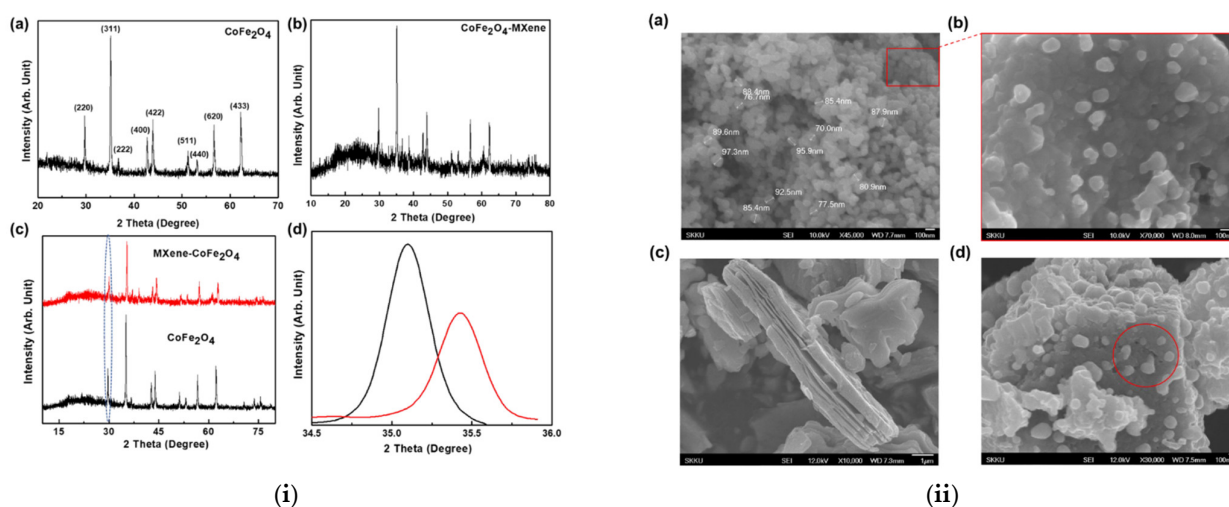


**Figure 10.** (**i**) XRD pattern of (**a**) Co ferrite, (**b**) MXene/Co-ferrite, (**c**) comparison pattern, and (**d**) magnified at lower angle, and (**ii**) SEM micrograph of (**a,b**) Co-ferrite, (**c**) MXene and (**d**) MXene/Co-ferrite nanocomposite. Reproduced with permission from [24] Copyright (2020) American Chemical Society.

The average layer thickness was estimated as 1 nm from atomic force microscopic experiments. The electrochemical supercapacitor analysis of the individual and nanocomposites were assessed in 1 M KOH electrolyte in a potential window of 0.0 to 0.5 V. The cyclic voltammogram curve shows the two distinct anodic and cathodic points, which might be due to the transition of $Fe^{2+}/Fe^{3+}$ and $Co^{2+}/Co^{3+}$ during the electrochemical redox reactions. The overall electrochemical reactions with the MXene/Co-ferrite nanocomposite were explained thorough the following reactions,

$$CoFe_2O_4 + H_2O + OH^- \rightarrow 2\ FeOOH + CoOOH + e^- \tag{3}$$

$$CoOOH + OH^- \rightarrow CoO_2 + H_2O + e^- \tag{4}$$

$$FeOOH + H_2O \rightarrow Fe(OH)_3 \rightarrow (FeO_4)^{2-} + 3e^- \tag{5}$$

The better electrochemical super capacitive performance was observed for MXene/Co-ferrite compared with bare Co-ferrite and MXene. The detailed electrochemical studies were carried out for the MXene/Co-ferrite nanocomposites. The CV curves were measured at the scan rate of 10 to 100 mV/s and the measured CV curves are shown in Figure 11a. The charge/discharge curves were measured at the current density of 1 to 8 A/g and the observed curves are shown in Figure 11b. The specific capacitance was estimated from the Galvanostatic charge-discharge (GCD) curves and calculated Cs values corresponding to its current densities are shown in Figure 11c. The highest Cs value of 1268 F/g was achieved at a current density of 1 A/g, whereas, with the same current density, bare Co-ferrite and MXene showed a specific capacitance value of 594 and 1046 F/g, respectively. The long-term cyclic stability was evidenced up to 5000 cycles with a current density of 7 A/g, and

the stability curve is shown in Figure 11d. The calculated specific capacity corresponding to its current densities is shown in Figure 11e. The highest specific capacity value of 440 C/g at a current density of 1 A/g was achieved with the lower charging transfer resistance values of 0.25 $\Omega$.
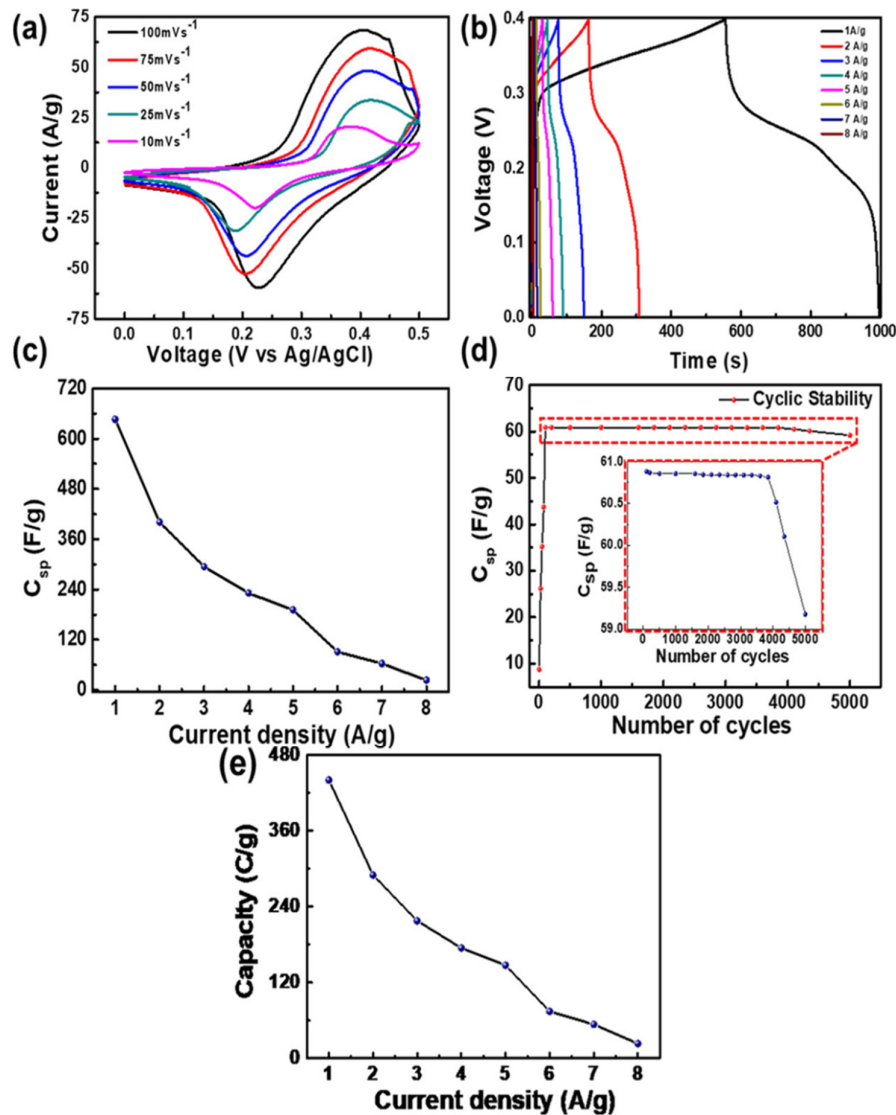


**Figure 11.** (**a**) CV, (**b**) GCD curves, (**c**) Cs vs. current density, (**d**) cyclic stability and (**e**) specific capacity vs. current density. Reproduced with permission from [24] Copyright (2020) American Chemical Society.

The observed electrochemical super capacitive characteristics of MXene/Co-ferrite indicate that these kinds of composites could be further investigated for the improvement in the specific capacitance and cyclic stability.

A recent study shows that the selection of electrolyte is also important for the MXene based ferrite composites [92]. The bare $Fe_3O_4$ and MXene/ $Fe_3O_4$ magnetic nanocomposites were developed through the modified chemical oxidation process by optimized experimental conditions. A few µm-sized MXenes and particle sizes ranging from 80 to 160 nm of $Fe_3O_4$ were evidenced from the microscopic measurements. The attachment of $Fe_3O_4$ on the MXene sheets in the MXene/$Fe_3O_4$ nanocomposite was evidenced from the TEM micrograph as shown in Figure 12.
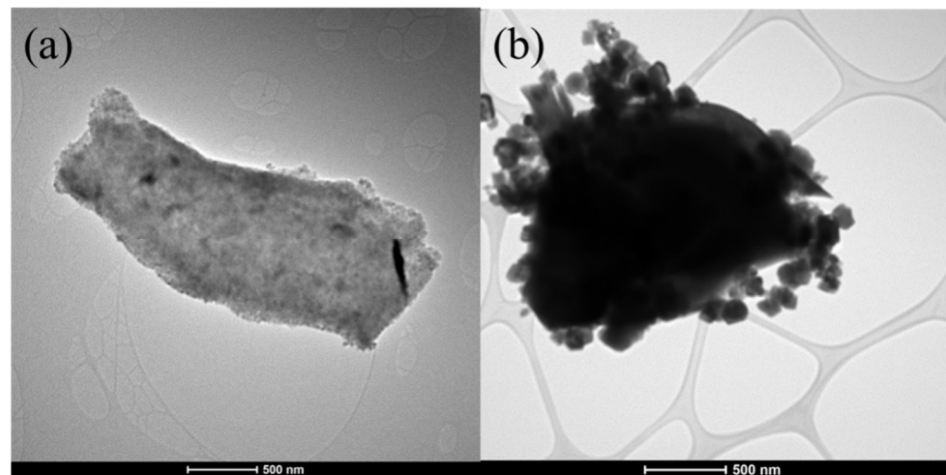
**Figure 12.** TEM Micrograph of (**a**) MXene, and (**b**) MXene/ $Fe_3O_4$.

Three electrolytes of LiCl, KOH and $Na_2SO_4$ were used to evaluate the suitable electrolyte for MXene/Ferrite composites with reduced graphene oxide. The measured CV, GCD curve are shown in Figure 13a,b. The higher area was observed for the nanocomposites characterized in LiCl electrolyte. Also, the LiCl showed better charge/discharge characteristics for MXene/$Fe_3O_4$ nanocomposite, compared with other two electrolytes. The estimated Cs with various current densities is shown in Figure 13c along with the EIS spectra in Figure 13d. The observed electrochemical performance demonstrated that the LiCl could provide better performance, which might be due a better combination of the lowest Li ion with the higher pore sizes in the MXene/ferrite composites. However, this electrolyte needs to be evaluated for other various combinations of MXene/ferrites to generalize the electrolyte characteristics.
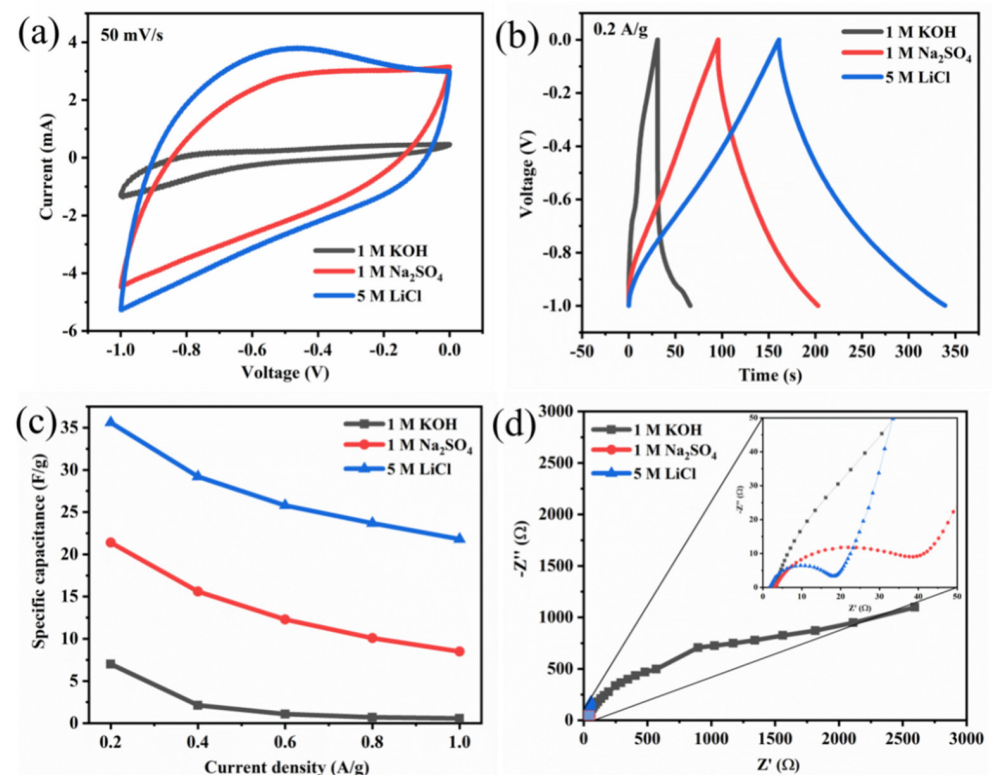


**Figure 13.** (**a**) CV, (**b**) GCD, (**c**) Cs vs. current density, and (**d**) EIS curves of MXene/$Fe_3O_4$.

## 4. Magnetic Field-assisted Applications

The external magnetic field can influence the electrochemical reactions, which is evidenced for different external magnetic fields in various electrolytes, electrodeposition of materials, and electrochemical applications [132–138]. It is expected that the magnetic field will be built as an effective system with the lowest energy consumption for large-scale applications through the continual and systematic development of this field [139–142]. Numerous investigations have demonstrated that the electron's energy state could be improved under a magnetic field. As a consequence, the improved energy state of the electrons would undoubtedly enhance the capacitance efficiency by increasing the effectiveness of electron movement at the electrolyte-electrode interface.

The experimental setup for the magnetic field-assisted supercapacitor applications can be easily constructed. The external magnetic field could be produced by two electromagnets, and the strength of the field could be controlled by adjusting the current supply to the electromagnets. The schematic experimental setup for the evaluation of role of the external magnetic field is shown in Figure 14. In the magnetic field produced by two electromagnets, a three-electrode cell should be immersed. To maintain consistent magnetic field intensity distribution between the positive and negative electrodes, the cell must be precisely placed. To assess the impact of the magnetic field, five different types of aqueous electrolytes, including NaOH, KOH, NaCl, $K_2SO_4$, and $H_2SO_4$ were tested [143]. On the working electrode, an amorphous commercial AC structure with significant microporosity was utilized.
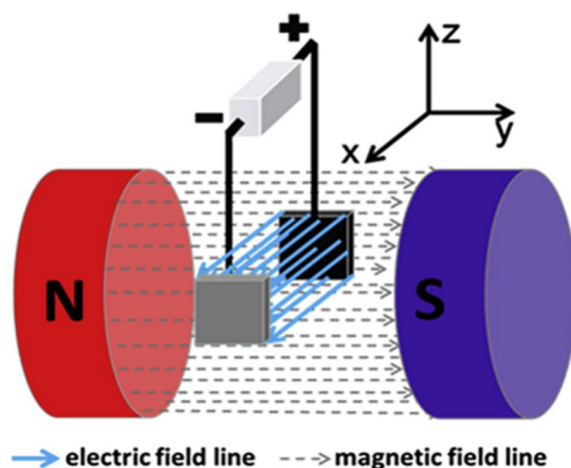


**Figure 14.** Schematic setup for the measurement of effect of external magnetic field. Reproduced (modified) from [143] Copyright (2021) with permission from Elsevier.

The various impacts of the magnetic field on the magnetocapacitance factor (MCF) values for NaOH, KOH, $H_2SO_4$, NaCl, and $K_2SO_4$ electrolytes with a magnetic field of 876 and 1786 Oe are summarized in Figure 15A,B. One may hypothesize that the active ions for rendering MCF are most likely proton and hydroxide ions by comparing $H_2SO_4$ and KOH with $K_2SO_4$ electrolytes (or by comparing NaOH with NaCl in the situation of the similar cation or anion). Without adding a magnetic field, the initial conductivities of the KOH, NaOH, and $H_2SO_4$ electrolyte were significantly higher than those of NaCl and $K_2SO_4$ electrolytes, as observed in Figure 15C. The KOH, NaOH, and $H_2SO_4$ electrolyte's conductivities linearly increased as the magnetic field's strength was amplified. Additionally, when the magnetic field was applied, the viscosity of all acidic and alkaline electrolytes decreased as observed in Figure 15D, which also contributes to the increase in conductivity. In contrast, in the magnetic field, the conductivities of $K_2SO_4$ and NaCl are barely changed. This may be because the neutral electrolyte does not clearly show the polarization impact of metal cations or anions in water.
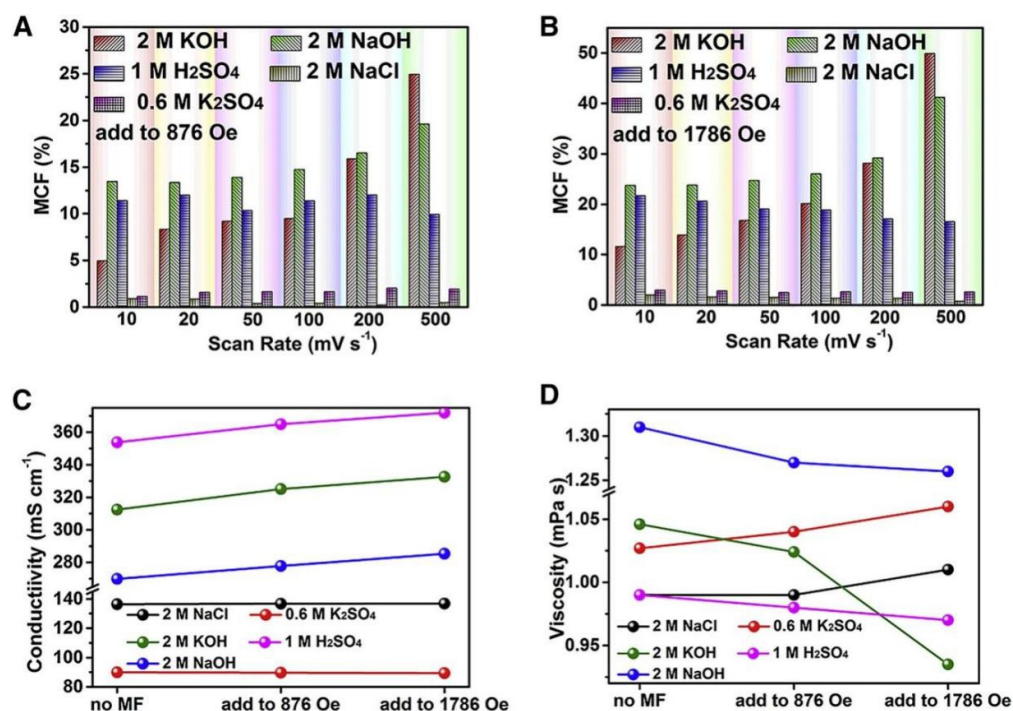
**Figure 15.** The impact of magnetic field on various aqueous electrolyte's conductivity, viscosity, and electrochemical properties. The MCF variation with scan rates under the magnetic field of (**A**) 876 Oe, and (**B**) 1786 Oe, (**C**) Variation in the conductivity with magnetic field, and (**D**)Variation in the viscosity with magnetic field. Reproduced (modified) from [143] Copyright (2021) with permission from Elsevier.

The impact of magnetic fields on the electrochemical behavior of KOH electrolytes at various concentrations was studied as shown in Figure 16A,B and compared the MCF values in KOH electrolytes of various concentrations at scan rates of 10 and 200 mV/s. The MCF values generally increased with concentration (6 M) at the slow scan rate of 10 mV/s, and the rise degree was more pronounced in the presence of a higher magnetic field. The MCF values, however, were nearly zero for concentrations of 8 and 10 M, independent of how strong the magnetic field was. When the concentrations were 1, 2, 4, and 6 M, however, the MCF values were positive at the relatively high rate of 200 mV/s. The MCF values, however, monotonously decreased as the concentration rose at a higher fraction of KOH (8 and 10 M). The original conductivity steadily increased with the rise in the fraction of KOH up to 8 M, as illustrated in Figure 16C. The conductivity decreased as the concentration was raised to 10 M, which is connected to the ions' delayed migration because of a high chance of ion collision and powerful electrostatic contact between anions and cations. The initial viscosity rose monotonously with the higher concentration, as seen in Figure 16D. When the electrolyte fraction was 1, 2, and 4 M, the magnetic field reduced the viscosity; however, in 6, 8, and 10 M KOH electrolytes, the viscosity rose. Concentrated electrolytes' decreased conductivity and increased viscosity in a magnetic field would hinder ion transport, which would affect the MCF readings. The limiting current density ($I_{lim}$) values derived from these Tafel polarization curves are displayed in Figure 16E. When compared to the initial outcomes obtained without adding the magnetic field, $I_{lim}$ enlarged little in the 1 and 2 M KOH electrolytes and significantly in the 4 M KOH electrolyte. $I_{lim}$ values, however, were lower than the initial values in electrolytes with 8 and 10 M KOH. The data above showed a relationship between $I_{lim}$, the concentration of electrolytes, and the strength of the magnetic field. The values of the diffusion coefficients for the various concentrated KOH electrolytes in various magnetic fields are shown in Figure 16F.
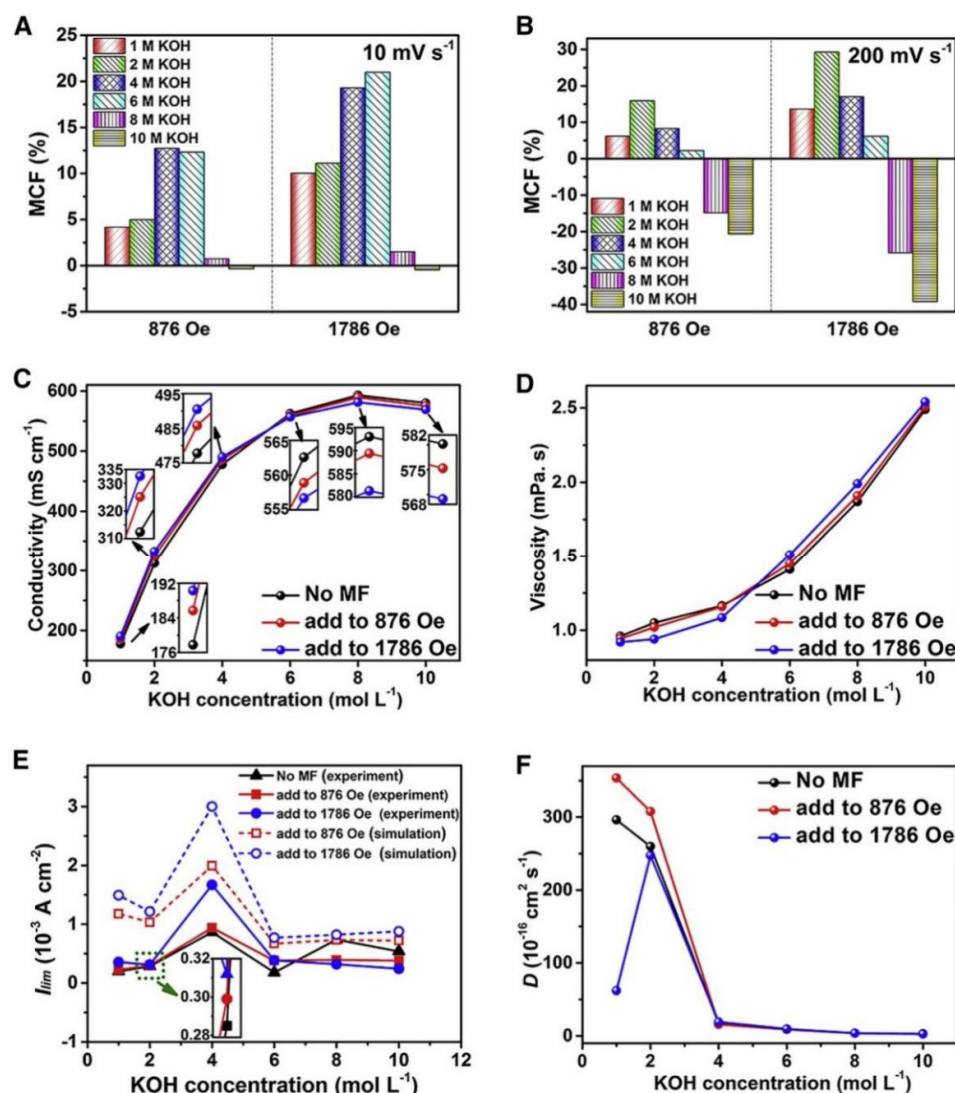
**Figure 16.** Influence of a magnetic field on the electrochemical properties of KOH electrolytes at various concentrations. Variation in the MCF values at a scan rate of (**A**) 10 mV/s, (**B**) 200 mV/s, (**C**) Variation in the conductivity with KOH concentrations under different magnetic field, (**D**) Variation in the viscosity with KOH concentrations under different magnetic field, (**E**) Variation of $I_{lim}$ with KOH concentrations, and (**F**) Diffusion coefficient of KOH with various concentrations. Reproduced (modified) from [143] Copyright (2021) with permission from Elsevier.

From the discussion, it is understood that the various magnetic forces acting on the electroactive ions cause solution convection at the electrolyte interface, which is the source of the magnetic field induced capacitance variation throughout the electrochemical reaction process. The fight among the driving force brought on by the Lorentz force and the damping force brought on by the conductivity of the electrolyte in KOH electrolytes is a key factor influencing the OH transport with the magnetic field. Whereas in the $H_2SO_4$ electrolyte, in addition to the previously mentioned forces, the third paramagnetic force produced by the paramagnetic $H^+$ under the magnetic field prevents the movement of $H^+$.

In a one-pot synthesis, $Fe_3O_4$/rGO nanocomposites were created by coupling the reduction of graphene oxide with the formation of $Fe_3O_4$ NPs under ambient conditions and utilized for a supercapacitor application with an external magnetic field to evaluate the influence of the external magnetic field [144]. $Fe_3O_4$ and $Fe_3O_4$/rGO hybrid symmetric two electrode electrochemical performance was examined utilizing CV and GCD measurements with an electrolyte of 1 M $Na_2SO_4$. With 0.125 T of the external magnetic field, the electrochemical performances of both electrodes have been explored (0.125 T).

Figure 17a,b shows the CV curves of $Fe_3O_4$ and $Fe_3O_4$/RGO in a magnetic field. These curves are substantially wider than those of the electrodes without a magnetic field, which were recorded at a scan rate of 5 mV/s, and show a greater specific capacitance. Figure 17c,d show the GCD curves of $Fe_3O_4$ and $Fe_3O_4$/RGO electrodes in the presence and absence of a magnetic field, respectively, at a current density of 0.1 A/g. Calculated Cs for ferrite and ferrite/rGO electrodes in a magnetic field are 303 and 869 F/g, respectively, at a scan rate of 5 mV/s. These values are 1.45 and 1.93 times greater than those of electrodes without using the field. These outcomes could be explained by enhanced electron transfer in the $Fe^{2+}$/$Fe^{3+}$ redox process in the materials with magnetic field exposure, which enhances the performance of devices by improving interface charge density, facilitating electrolyte transportation, and promoting cation intercalation/de-intercalation performance.
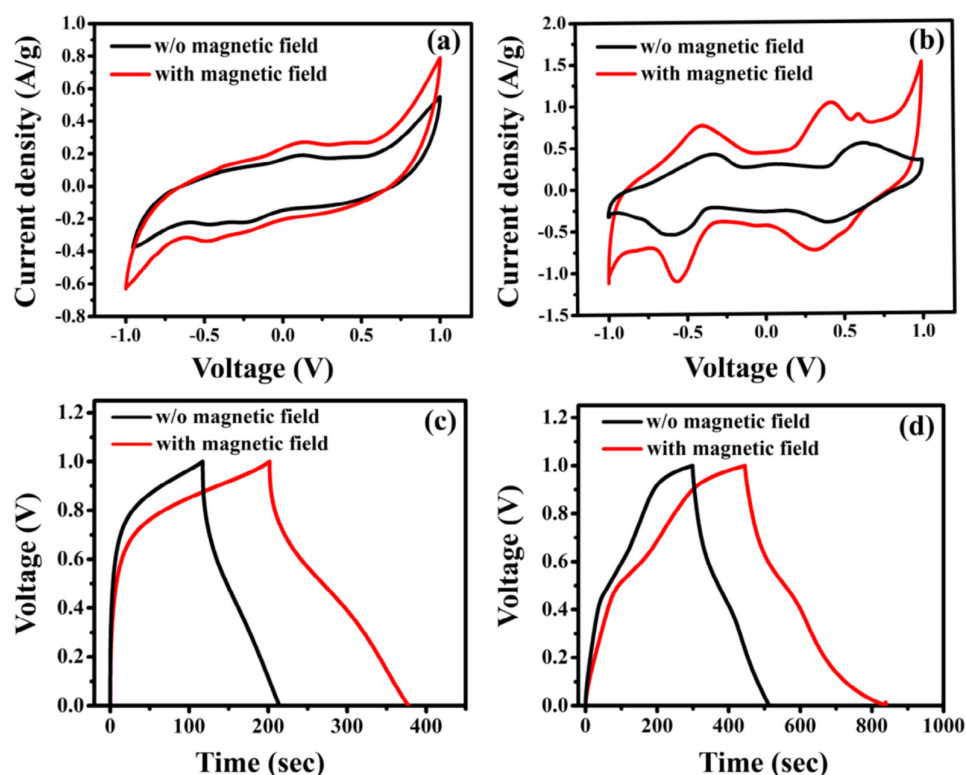


**Figure 17.** CV and GCD curves of (**a,c**) $Fe_3O_4$ and (**b,d**) $Fe_3O_4$/RGO with and without magnetic field. Reproduced with permission from [144] Copyright (2018) IOP Publishing.

The thermal decomposition approach was used to create consistently sized $Fe_2O_3$ nanoparticles with sizes between 12 and 30 nm for the graphene surface [145]. Decorating of the non-conductive $Fe_2O_3$, the capacitance performance of the $Fe_2O_3$/graphene nanocomposite is significantly decreased because of the higher internal resistance and poor electron transportation efficiency. The electrochemical supercapacitive characteristics were analyzed with 1.0 M $Na_2SO_4$ and the external magnetic field of 720 Gauss. The measured CV curves for bare $Fe_2O_3$ and $Fe_2O_3$/graphene nanocomposites with the external magnetic field are shown in Figure 18a–d.

The Cs of graphene is considerably increased by 67 and 27% at 2 and 10 mV/s, respectively, after positioning the electrode in an external magnetic field. At 2 and 10 mV/s, the $Fe_2O_3$/graphene nanocomposite displays an enhancement that is much greater by 154.6 and 98.2%. The estimated energy density and current density for bare $Fe_2O_3$ and $Fe_2O_3$/graphene nanocomposites are shown in Figure 19a,b. Equivalent circuit modeling of EIS shows a significant amount of leakage resistance between the electrode-electrolyte line caused by a relaxation progression at low frequency. By applying a small magnetic field, this relaxation process was considerably restrained, effectively increasing the capacitor output.

These findings provide a novel method for improving the electrochemical capacitors now in use by merely introducing an external magnetic field. We could utilize the specific response from any magnetic or nonmagnetic materials, which could be utilized to influence various applications of nanomaterials. The influence of the external magnetic field on various applications is listed in Table 3.
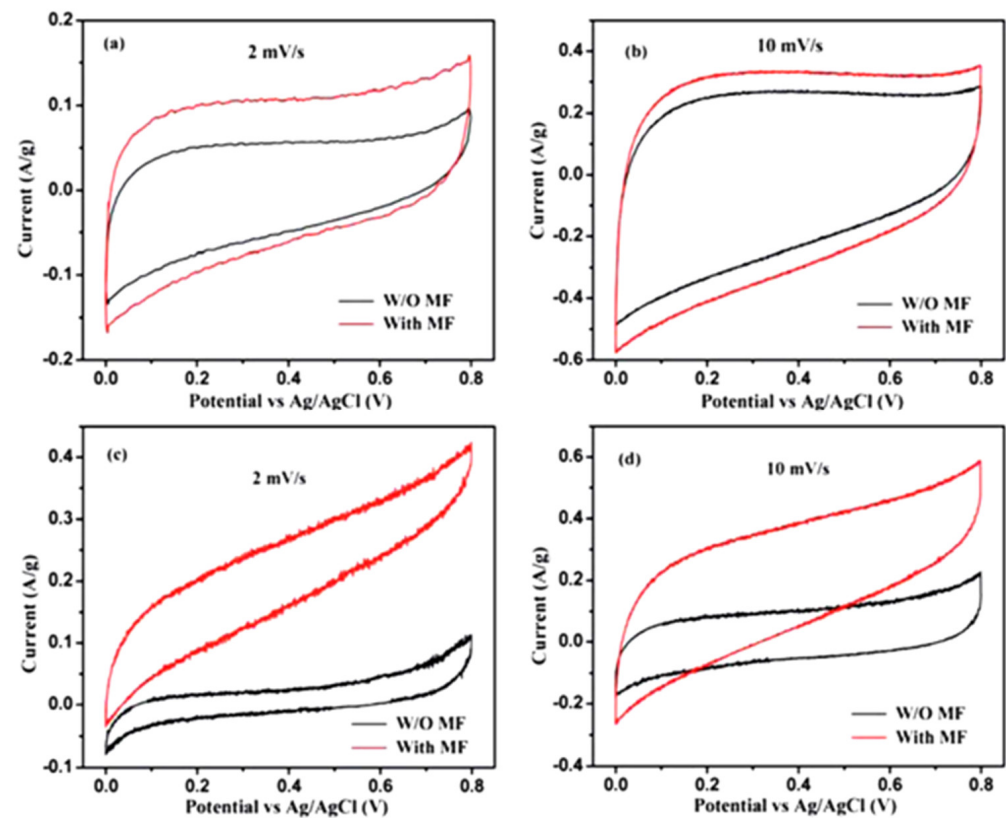


**Figure 18.** CV curves of (**a,b**) $Fe_2O_3$ and (**c,d**) $Fe_2O_3$/graphene. Reproduced with permission from [145] Copyright (2012) Royal Society of Chemistry.
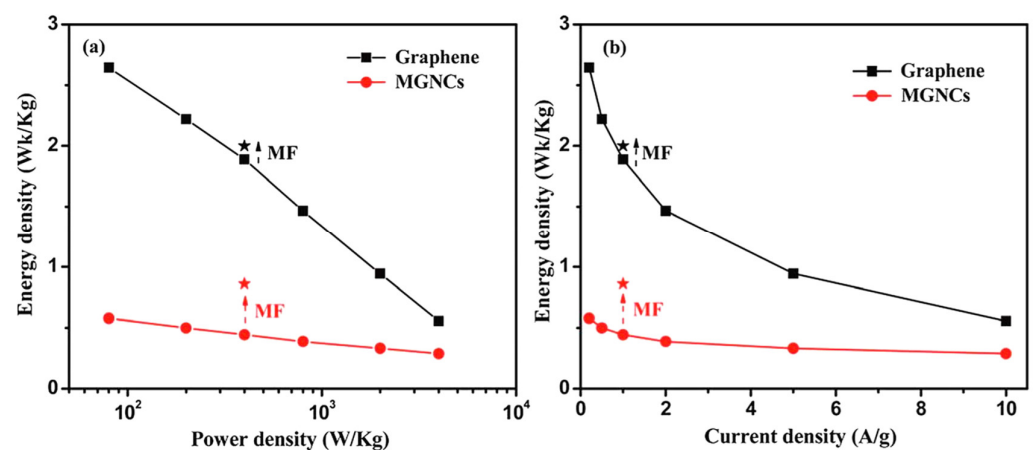


**Figure 19.** Energy density vs. (**a**) power density and (**b**) current density of graphene and $Fe_2O_3$/graphene composite. Reproduced with permission from [145] Copyright (2012) Royal Society of Chemistry.

**Table 3.** Utilization of external magnetic field for the synthesis and applications.

| S. No | Materials | Magnetic Field (T) | Synthesis/Applications | Improved Efficiency (%) | Ref. |
|---|---|---|---|---|---|
| 1 | $FeCo_2O_4$ | 3 mT | supercapacitor | 56 | [146] |
| 2 | $AC/Fe_3O_4$ | – | supercapacitor | 33.1 | [147] |
| 3 | $Fe_3O_4/PPy$ | 0.1 T | supercapacitor | 128 | [148] |
| 4 | $Mn_3O_4$ | Up to 3 mT | supercapacitor | 50 | [149] |
| 5 | Nanoporous nickel | 500 mT | supercapacitor | ~12 | [150] |
| 6 | $Graphene/Fe_2O_3$ | 72 mT | supercapacitor | 154 | [145] |
| 7 | Graphene oxide anchored $Fe_3O_4$ | 0.125 T | supercapacitor | 193 | [144] |
| 8 | $FeCo_2O_4$ | 3 mT | supercapacitor | ~21 | [151] |
| 9 | Flexible magnetic Microtubule nanocomposite fabrics ((Iron, Nickel, Cobalt) with carbon) | 72 mT | supercapacitor | 70 | [152] |
| 10 | Ferromagnetic metal oxide -$Fe_2O_3$ | 0 to 5 mT | supercapacitors | 170 | [153] |
| 11 | $Co_3V_2O_8$-RGO | 0.5 T | supercapacitors | ~170 | [154] |
| 12 | NiCo-graphene quantum dot | – | supercapacitor | - | [155] |
| 13 | $MnO_2$-electrospun carbon nanofibers | 1.34 mT | supercapacitor | 19 | [156] |
| 14 | $\alpha$-$Fe_2O_3$/N-doped carbon | 0.15 T | Li-ion battery | 45 | [157] |
| 15 | KCl, KBr, KI, $Na_2SO_4$, and $CH_3COOH$ | 15 mT | improvement in conductivity | - | [158] |
| 16 | Iron | 0.6 T | ferromagnetic electrodes | - | [159] |
| 17 | Water-electrolyte solution | 0.42 T | Ion-Exchange Kinetics | - | [160] |
| 18 | $Fe_3O_4/TiO_2$ | Up to 80 mT | photocatalysis | ~200 | [161] |
| 19 | $ZnFe_2O_4$ | Up to 0.8 T | photocatalysis | 150 | [162] |
| 20 | $\alpha$-$Fe_2O_3$-decorated $TiO_2$ nanotube arrays | 0.4 T | photocatalysis | ~38 | [163] |
| 21 | Au-CdS | Up to 81 mT | photocatalytic hydrogen production | 110 | [164] |
| 22 | $TiO_2$ | 0.28 T | photodegradation of methyl orange | 24 | [165] |
| 23 | Palladium | 0.5 T | catalytic activity in Suzuki cross-coupling reactions | 50 | [166] |
| 24 | Copper metal ions | 0.685 T | magneto electrolysis | - | [167] |
| 25 | $NiZnFe_4O_x$ | $\leq$ 450 mT | electrocatalytic water oxidation | 100 | [168] |
| 26 | AgAu | 450 mT | electrochemical dealloying | With MF − 0.5 cycles and without MF > 1.5 cycles | [169] |

**Table 3.** *Cont.*

| S. No | Materials | Magnetic Field (T) | Synthesis/Applications | Improved Efficiency (%) | Ref. |
|-------|-----------|--------------------|------------------------|-------------------------|------|
| 27 | NiO on nickel foam | 0–12.6 mT | magnetic-field-assisted hydrothermal method | - | [170] |
| 28 | Copper | 0.4 to 1 T | electrodeposition | - | [171] |
| 29 | Silver | 1.2 T | electrodeposition | - | [172] |
| 30 | Nickel | 1 T | electrodeposition | - | [173] |
| 31 | Cobalt | 0–5 T | electrodeposition | - | [174] |
| 32 | Nickel | 0.7 T | electrodeposition | - | [175] |
| 33 | Cobalt hydroxides | 2 T | phase engineering | - | [176] |

From the above discussions, we observed that the external magnetic field can influence the electrochemical performance of the electrolyte. On the other hand, when we use the magnetic nanomaterials as supercapacitive electrode materials, the supercapacitive performance is influenced by the external magnetic field, as the magnetic electrode materials could easily respond to the applied magnetic field. The external magnetic field may increase or decrease the electrochemical performance of the supercapacitive electrode materials subject to the magnetic nature of the materials. Also, the amount of magnetic field used as external magnetic field can influence the electrochemical supercapacitive characteristics of the magnetic electrode materials. This discussion does not conclude that the rise in field strength can increase the supercapacitive performance. The supercapacitive performance of the magnetic materials depends on the particle size, shape, magnetic characteristics of the materials, and the external magnetic field strength. Limited reports are only available on the evaluation of the magnetic field effect on the supercapacitive performance of the magnetic materials. The combinations of MXene with ferrites should be investigated further with various forms of MXenes, ferrites, and further investigation could be done under the external magnetic field.

## 5. Summary, Scope, and Future Perspective

The synthesis process for the MXene, Ferrites and MXene/Ferrite magnetic nanocomposites was briefly discussed. The importance of attachment of the ferrite on the layers of MXenes was studied. The recent progress on MXene/ferrite formation through chemical reaction was reviewed with $Fe_3O_4$ and $CoFe_2O_4$. The importance of the selection of a suitable electrolyte was analyzed with the result of MXene/$Fe_3O_4$ magnetic nanocomposites. The external magnetic field plays an important role in the tuning of electrochemical characteristics of the electrolyte, as well as electrode materials. The role of the external magnetic field on the electrolytes was discussed with KOH, NaOH, NaCl, $K_2SO_4$, and $H_2SO_4$ electrolytes with 876 and 1786 Oe of magnetic field. Furthermore, we provided a detailed analysis of the effect of the amount of KOH electrolyte with the external magnetic field. The schematic preparation process and magnetic field-assisted electrochemical supercapacitor application is shown in Figure 20.

There are lots of issues related to the synthesis of scalable and single phase MXene through top down as well from the bottom approach methods. Present research could make the challenges into opportunities to explore further on the synthesis of MXene without any impurity or secondary phase. Several strategies are also demonstrated to have a stable MXene by avoiding oxidation/degradation. However, the formation of single phase, stoichiometry variation through synthesis process, shape and size of ferrites can be varied depending on the requirement as the well-established procedures and discussions were available for various ferrites. There are numerous ferrites with different stoichiometry need to be explored for the formation of magnetic nanocomposites with MXene. Several chemical reaction processes also to be optimized for the better formation of nanocomposite

with required physicochemical interaction. Green synthesis methods could also be adopted for the development of magnetic hybrid composites with MXene. By optimizing the experimental parameters such as starting precursors, reaction time, reaction temperature and post thermal treatment we could be able to achieve the perfect nanocomposites of MXene and ferrite without any agglomeration. The effect of magnetic field on the electrochemical characterization of MXene/Ferrite nanocomposite are open to be explore further for the next generation supercapacitor applications as there are more opportunities to tune the magnetic materials shape, size, magnetic characteristics, and the strength of magnetic field. Analyses of studies that have already been published, hint at this field of study's potential significance. However, there are still many unexplored facets of the magnetic field influence on electrochemical applications which needs attention.
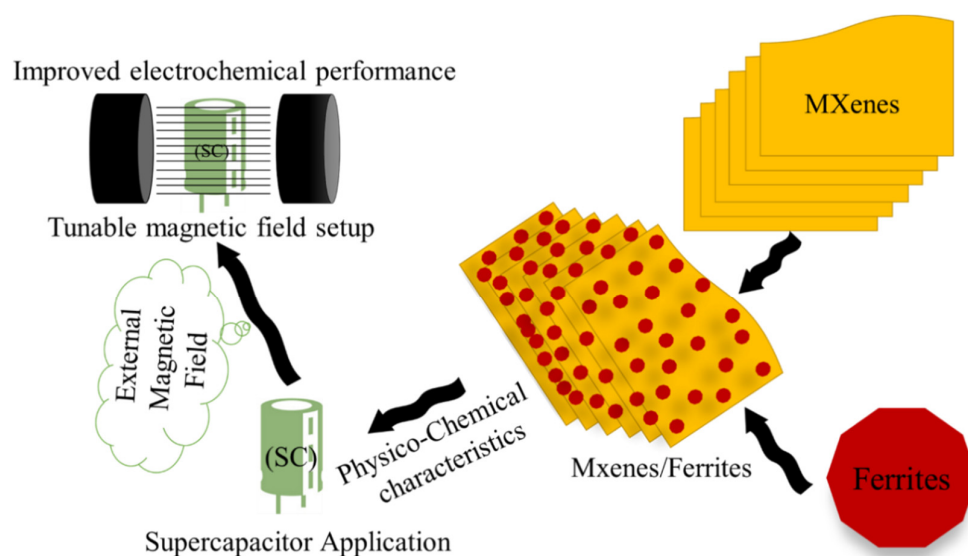


**Figure 20.** Schematic process diagram for the magnetic field assisted supercapacitor application with MXene/Ferrite magnetic nanocomposites.

**Author Contributions:** Conceptualization, A.T. and A.R., writing—original draft preparation, A.T., S.S.D. and S.-K.K. writing—review and editing, N.C., S.G. and C.V.A., supervision, R.U., M.J.M. and Y.A.R.C. All authors have read and agreed to the published version of the manuscript.

## References

1. Chen, Y.; Yang, H.; Han, Z.; Bo, Z.; Yan, J.; Cen, K.; Ostrikov, K.K. MXene-Based Electrodes for Supercapacitor Energy Storage. *Energy Fuels* **2022**, *36*, 2390–2406. [CrossRef]
2. Zhan, C.; Naguib, M.; Lukatskaya, M.; Kent, P.R.C.; Gogotsi, Y.; Jiang, D.E. Understanding the MXene Pseudocapacitance. *J. Phys. Chem. Lett.* **2018**, *9*, 1223–1228. [CrossRef] [PubMed]
3. Okubo, M.; Sugahara, A.; Kajiyama, S.; Yamada, A. MXene as a Charge Storage Host. *Acc. Chem. Res.* **2018**, *51*, 591–599. [CrossRef] [PubMed]
4. Gogotsi, Y.; Anasori, B. The Rise of MXenes. *ACS Nano* **2019**, *13*, 8491–8494. [CrossRef] [PubMed]
5. Naguib, M.; Mochalin, V.N.; Barsoum, M.W.; Gogotsi, Y. 25th Anniversary Article: MXenes: A New Family of Two-Dimensional Materials. *Adv. Mater.* **2014**, *26*, 992–1005. [CrossRef] [PubMed]

6.  Mu, X.; Wang, D.; Du, F.; Chen, G.; Wang, C.; Wei, Y.; Gogotsi, Y.; Gao, Y.; Dall'Agnese, Y. Revealing the Pseudo-Intercalation Charge Storage Mechanism of MXenes in Acidic Electrolyte. *Adv. Funct. Mater.* **2019**, *29*, 1902953. [CrossRef]

7.  Anasori, B.; Lukatskaya, M.R.; Gogotsi, Y. 2D Metal Carbides and Nitrides (MXenes) for Energy Storage. *Nat. Rev. Mater.* **2017**, *2*, 16098. [CrossRef]

8.  Ling, Z.; Ren, C.E.; Zhao, M.Q.; Yang, J.; Giammarco, J.M.; Qiu, J.; Barsoum, M.W.; Gogotsi, Y. Flexible and Conductive MXene Films and Nanocomposites with High Capacitance. *Proc. Natl. Acad. Sci. USA* **2014**, *111*, 16676–16681. [CrossRef]

9.  Kurra, N.; Ahmed, B.; Gogotsi, Y.; Alshareef, H.N. MXene-on-Paper Coplanar Microsupercapacitors. *Adv. Energy Mater.* **2016**, *6*, 1601372. [CrossRef]

10. Ghidiu, M.; Naguib, M.; Shi, C.; Mashtalir, O.; Pan, L.M.; Zhang, B.; Yang, J.; Gogotsi, Y.; Billinge, S.J.L.; Barsoum, M.W. Synthesis and Characterization of Two-Dimensional $Nb_4C_3$ (MXene). *Chem. Commun.* **2014**, *50*, 9517–9520. [CrossRef]

11. Zhu, Q.; Li, J.; Simon, P.; Xu, B. Two-Dimensional MXenes for Electrochemical Capacitor Applications: Progress, Challenges and Perspectives. *Energy Storage Mater.* **2021**, *35*, 630–660. [CrossRef]

12. Das, P.; Wu, Z.S. MXene for Energy Storage: Present Status and Future Perspectives. *J. Phys. Energy* **2020**, *2*, 032004. [CrossRef]

13. Ando, Y.; Okubo, M.; Yamada, A.; Otani, M. Capacitive versus Pseudocapacitive Storage in MXene. *Adv. Funct. Mater.* **2020**, *30*, 2000820. [CrossRef]

14. Xu, J.; Hu, X.; Wang, X.; Wang, X.; Ju, Y.; Ge, S.; Lu, X.; Ding, J.; Yuan, N.; Gogotsi, Y. Low-Temperature Pseudocapacitive Energy Storage in $Ti_3C_2Tx$ MXene. *Energy Storage Mater.* **2020**, *33*, 382–389. [CrossRef]

15. Wang, T.; Zhao, J.; Qi, L.; Li, G.; Yang, W.; Li, Y. Ultrathin Graphdiyne Oxide-Intercalated MXene: A New Heterostructure with Interfacial Synergistic Effect for High Performance Lithium-Ion Storage. *Energy Storage Mater.* **2023**, *54*, 10–19. [CrossRef]

16. Li, J.; Yuan, X.; Lin, C.; Yang, Y.; Xu, L.; Du, X.; Xie, J.; Lin, J.; Sun, J. Achieving High Pseudocapacitance of 2D Titanium Carbide (MXene) by Cation Intercalation and Surface Modification. *Adv. Energy Mater.* **2017**, *7*, 1602725. [CrossRef]

17. Nithya, V.D.; Sabari Arul, N. Progress and Development of $Fe_3O_4$ Electrodes for Supercapacitors. *J. Mater. Chem. A* **2016**, *4*, 10767–10778. [CrossRef]

18. Arun, T.; Kavin Kumar, T.; Udayabhaskar, R.; Morel, M.J.; Rajesh, G.; Mangalaraja, R.V.; Akbari-Fakhrabadi, A. Size Dependent Magnetic and Capacitive Performance of $MnFe_2O_4$ Magnetic Nanoparticles. *Mater. Lett.* **2020**, *276*, 128240. [CrossRef]

19. Nwodo, M.O.; Obodo, R.M.; Nwanya, A.C.; Ekwealor, A.B.C.; Ezema, F.I. Recent Developments in Metal Ferrite Materials for Supercapacitor Applications. In *Electrode Materials for Energy Storage and Conversion*; CRC Press: Boca Raton, FL, USA; Taylor & Francis Group: London, UK, 2021; pp. 171–212. [CrossRef]

20. Arun, T.; Kavinkumar, T.; Udayabhaskar, R.; Kiruthiga, R.; Morel, M.J.; Aepuru, R.; Dineshbabu, N.; Ravichandran, K.; Akbari-Fakhrabadi, A.; Mangalaraja, R.V. $NiFe_2O_4$ Nanospheres with Size-Tunable Magnetic and Electrochemical Properties for Superior Supercapacitor Electrode Performance. *Electrochim. Acta* **2021**, *399*, 139346. [CrossRef]

21. Naguib, M.; Barsoum, M.W.; Gogotsi, Y. Ten Years of Progress in the Synthesis and Development of MXenes. *Adv. Mater.* **2021**, *33*, 2103393. [CrossRef]

22. Verger, L.; Natu, V.; Carey, M.; Barsoum, M.W. MXenes: An Introduction of Their Synthesis, Select Properties, and Applications. *Trends Chem.* **2019**, *1*, 656–669. [CrossRef]

23. Kumar, S.; Kumar, P.; Singh, N.; Kansal, M.K.; Kumar, A.; Verma, V. Highly Efficient and Sustainable MXene Based Heterostructure Composites Filled with Ferrites and MWCNTs to Mitigate the Radiation Interference in X-Band Frequency Region. *Mater. Sci. Eng. B* **2022**, *282*, 115798. [CrossRef]

24. Ayman, I.; Rasheed, A.; Ajmal, S.; Rehman, A.; Ali, A.; Shakir, I.; Warsi, M.F. CoFe2O4 Nanoparticle-Decorated 2D MXene: A Novel Hybrid Material for Supercapacitor Applications. *Energy Fuels* **2020**, *34*, 7622–7630. [CrossRef]

25. Arun, T.; Dhanabalan, S.S.; Udayabhaskar, R.; Ravichandran, K.; Akbari-Fakhrabadi, A.; Morel, M.J.; Arun, T.; Dhanabalan, S.S.; Akbari-Fakhrabadi, A.; Morel, M.J. *Magnetic Nanomaterials for Energy Storage Applications*; Springer: Cham, Switzerland, 2022; pp. 131–150.

26. Guo, Z.; Ren, P.; Lu, Z.; Hui, K.; Yang, J.; Zhang, Z.; Chen, Z.; Jin, Y.; Ren, F. Multifunctional CoFe2O4@MXene-AgNWs/Cellulose Nanofiber Composite Films with Asymmetric Layered Architecture for High-Efficiency Electromagnetic Interference Shielding and Remarkable Thermal Management Capability. *ACS Appl. Mater. Interfaces* **2022**, *14*, 41468–41480. [CrossRef] [PubMed]

27. Yang, X.; Liu, Y.; Hu, S.; Yu, F.; He, Z.; Zeng, G.; Feng, Z.; Sengupta, A. Construction of $Fe_3O_4$@MXene Composite Nanofiltration Membrane for Heavy Metal Ions Removal from Wastewater. *Polym. Adv. Technol.* **2021**, *32*, 1000–1010. [CrossRef]

28. Xu, J.; Zeng, G.; Lin, Q.; Gu, Y.; Wang, X.; Feng, Z.; Sengupta, A. Application of 3D Magnetic Nanocomposites: MXene-Supported $Fe_3O_4$@CS Nanospheres for Highly Efficient Adsorption and Separation of Dyes. *Sci. Total Environ.* **2022**, *822*, 153544. [CrossRef] [PubMed]

29. Zhang, Z.; Wang, B.; Han, R.; Jin, F.; Zhang, N.; Zhang, T.; Wang, D. 3D Alk-MXene@$Fe_3O_4$ as Cathode Additive for Rechargeable Lithium−Sulfur Batteries. *Adv. Energy Sustain. Res.* **2022**, *3*, 2100167. [CrossRef]

30. Thirumurugan, A.; Akbari-Fakhrabadi, A.; Joseyphus, R.J. Surface Modification of Highly Magnetic Nanoparticles for Water Treatment to Remove Radioactive Toxins. In *Green Methods for Wastewater Treatment*; Springer: Cham, Switzerland, 2020; pp. 31–54. [CrossRef]

31. Jiang, L.; Zhou, D.; Yang, J.; Zhou, S.; Wang, H.; Yuan, X.; Liang, J.; Li, X.; Chen, Y.; Li, H. 2D Single- and Few-Layered MXenes: Synthesis, Applications and Perspectives. *J. Mater. Chem. A* **2022**, *10*, 13651–13672. [CrossRef]

32. Verger, L.; Xu, C.; Natu, V.; Cheng, H.M.; Ren, W.; Barsoum, M.W. Overview of the Synthesis of MXenes and Other Ultrathin 2D Transition Metal Carbides and Nitrides. *Curr. Opin. Solid State Mater. Sci.* **2019**, *23*, 149–163. [CrossRef]

33. Gao, L.; Li, C.; Huang, W.; Mei, S.; Lin, H.; Ou, Q.; Zhang, Y.; Guo, J.; Zhang, F.; Xu, S.; et al. MXene/Polymer Membranes: Synthesis, Properties, and Emerging Applications. *Chem. Mater.* **2020**, *32*, 1703–1747. [CrossRef]

34. Shuck, C.E.; Sarycheva, A.; Anayee, M.; Levitt, A.; Zhu, Y.; Uzun, S.; Balitskiy, V.; Zahorodna, V.; Gogotsi, O.; Gogotsi, Y. Scalable Synthesis of Ti$_3$C$_2$Tx MXene. *Adv. Eng. Mater.* **2020**, *22*, 1901241. [CrossRef]

35. Naguib, M.; Mashtalir, O.; Carle, J.; Presser, V.; Lu, J.; Hultman, L.; Gogotsi, Y.; Barsoum, M.W. Two-Dimensional Transition Metal Carbides. *ACS Nano* **2012**, *6*, 1322–1331. [CrossRef]

36. Naguib, M.; Kurtoglu, M.; Presser, V.; Lu, J.; Niu, J.; Heon, M.; Hultman, L.; Gogotsi, Y.; Barsoum, M.W. Two-Dimensional Nanocrystals Produced by Exfoliation of Ti$_3$AlC$_2$. *Adv. Mater.* **2011**, *23*, 4248–4253. [CrossRef]

37. Sang, X.; Xie, Y.; Lin, M.W.; Alhabeb, M.; Van Aken, K.L.; Gogotsi, Y.; Kent, P.R.C.; Xiao, K.; Unocic, R.R. Atomic Defects in Monolayer Titanium Carbide (Ti$_3$C$_2$Tx) MXene. *ACS Nano* **2016**, *10*, 9193–9200. [CrossRef]

38. Xuan, J.; Wang, Z.; Chen, Y.; Liang, D.; Cheng, L.; Yang, X.; Liu, Z.; Ma, R.; Sasaki, T.; Geng, F.; et al. Organic-Base-Driven Intercalation and Delamination for the Production of Functionalized Titanium Carbide Nanosheets with Superior Photothermal Therapeutic Performance. *Angew. Chemie Int. Ed.* **2016**, *55*, 14569–14574. [CrossRef]

39. Ghidiu, M.; Lukatskaya, M.R.; Zhao, M.Q.; Gogotsi, Y.; Barsoum, M.W. Conductive Two-Dimensional Titanium Carbide 'Clay' with High Volumetric Capacitance. *Nature* **2014**, *516*, 78–81. [CrossRef]

40. Lipatov, A.; Alhabeb, M.; Lukatskaya, M.R.; Boson, A.; Gogotsi, Y.; Sinitskii, A.; Lipatov, A.; Boson, A.; Sinitskii, A.; Alhabeb, M.; et al. Effect of Synthesis on Quality, Electronic Properties and Environmental Stability of Individual Monolayer Ti$_3$C$_2$ MXene Flakes. *Adv. Electron. Mater.* **2016**, *2*, 1600255. [CrossRef]

41. Li, M.; Lu, J.; Luo, K.; Li, Y.; Chang, K.; Chen, K.; Zhou, J.; Rosen, J.; Hultman, L.; Eklund, P.; et al. Element Replacement Approach by Reaction with Lewis Acidic Molten Salts to Synthesize Nanolaminated MAX Phases and MXenes. *J. Am. Chem. Soc.* **2019**, *141*, 4730–4737. [CrossRef]

42. Halim, J.; Lukatskaya, M.R.; Cook, K.M.; Lu, J.; Smith, C.R.; Näslund, L.Å.; May, S.J.; Hultman, L.; Gogotsi, Y.; Eklund, P.; et al. Transparent Conductive Two-Dimensional Titanium Carbide Epitaxial Thin Films. *Chem. Mater.* **2014**, *26*, 2374–2381. [CrossRef]

43. Kamysbayev, V.; Filatov, A.S.; Hu, H.; Rui, X.; Lagunas, F.; Wang, D.; Klie, R.F.; Talapin, D.V. Covalent Surface Modifications and Superconductivity of Two-Dimensional Metal Carbide MXenes. *Science* **2020**, *369*, 979–983. [CrossRef]

44. Li, T.; Yao, L.; Liu, Q.; Gu, J.; Luo, R.; Li, J.; Yan, X.; Wang, W.; Liu, P.; Chen, B.; et al. Fluorine-Free Synthesis of High-Purity Ti$_3$C$_2$Tx (T=OH, O) via Alkali Treatment. *Angew. Chemie Int. Ed.* **2018**, *57*, 6115–6119. [CrossRef]

45. Mashtalir, O.; Naguib, M.; Mochalin, V.N.; Dall'Agnese, Y.; Heon, M.; Barsoum, M.W.; Gogotsi, Y. Intercalation and Delamination of Layered Carbides and Carbonitrides. *Nat. Commun.* **2013**, *4*, 1716. [CrossRef]

46. Naguib, M.; Unocic, R.R.; Armstrong, B.L.; Nanda, J. Large-Scale Delamination of Multi-Layers Transition Metal Carbides and Carbonitrides "MXenes". *Dalt. Trans.* **2015**, *44*, 9353–9358. [CrossRef]

47. Liu, F.; Zhou, A.; Chen, J.; Jia, J.; Zhou, W.; Wang, L.; Hu, Q. Preparation of Ti3C2 and Ti2C MXenes by Fluoride Salts Etching and Methane Adsorptive Properties. *Appl. Surf. Sci.* **2017**, *416*, 781–789. [CrossRef]

48. Zhang, C.J.; Pinilla, S.; McEvoy, N.; Cullen, C.P.; Anasori, B.; Long, E.; Park, S.H.; Seral-Ascaso, A.; Shmeliov, A.; Krishnan, D.; et al. Oxidation Stability of Colloidal Two-Dimensional Titanium Carbides (MXenes). *Chem. Mater.* **2017**, *29*, 4848–4856. [CrossRef]

49. Iqbal, A.; Hong, J.; Ko, T.Y.; Koo, C.M. Improving Oxidation Stability of 2D MXenes: Synthesis, Storage Media, and Conditions. *Nano Converg.* **2021**, *8*, 9. [CrossRef]

50. Habib, T.; Zhao, X.; Shah, S.A.; Chen, Y.; Sun, W.; An, H.; Lutkenhaus, J.L.; Radovic, M.; Green, M.J. Oxidation Stability of Ti$_3$C$_2$Tx MXene Nanosheets in Solvents and Composite Films. *NPJ 2D Mater. Appl.* **2019**, *3*, 8. [CrossRef]

51. Cao, F.; Zhang, Y.; Wang, H.; Khan, K.; Tareen, A.K.; Qian, W.; Zhang, H.; Ågren, H. Recent Advances in Oxidation Stable Chemistry of 2D MXenes. *Adv. Mater.* **2022**, *34*, 2107554. [CrossRef]

52. Fan, Q.; Yi, M.; Chai, C.; Li, W.; Qi, P.; Wang, J.; Hao, J. Oxidation Stability Enhanced MXene-Based Porous Materials Derived from Water-in-Ionic Liquid Pickering Emulsions for Wearable Piezoresistive Sensor and Oil/Water Separation Applications. *J. Colloid Interface Sci.* **2022**, *618*, 311–321. [CrossRef]

53. Harzali, H.; Saida, F.; Marzouki, A.; Megriche, A.; Baillon, F.; Espitalier, F.; Mgaidi, A. Structural and Magnetic Properties of Nano-Sized NiCuZn Ferrites Synthesized by Co-Precipitation Method with Ultrasound Irradiation. *J. Magn. Magn. Mater.* **2016**, *419*, 50–56. [CrossRef]

54. Wang, J.; Ren, F.; Yi, R.; Yan, A.; Qiu, G.; Liu, X. Solvothermal Synthesis and Magnetic Properties of Size-Controlled Nickel Ferrite Nanoparticles. *J. Alloys Compd.* **2009**, *479*, 791–796. [CrossRef]

55. Yue, Z.; Guo, W.; Zhou, J.; Gui, Z.; Li, L. Synthesis of Nanocrystalline Ferrites by Sol–Gel Combustion Process: The Influence of PH Value of Solution. *J. Magn. Magn. Mater.* **2004**, *270*, 216–223. [CrossRef]

56. Arun, T.; Prakash, K.; Kuppusamy, R.; Joseyphus, R.J. Magnetic Properties of Prussian Blue Modified Fe$_3$O$_4$ Nanocubes. *J. Phys. Chem. Solids* **2013**, *74*, 1761–1768. [CrossRef]

57. Töpfer, J.; Angermann, A. Nanocrystalline Magnetite and Mn–Zn Ferrite Particles via the Polyol Process: Synthesis and Magnetic Properties. *Mater. Chem. Phys.* **2011**, *129*, 337–342. [CrossRef]

58. Melo, R.S.; Silva, F.C.; Moura, K.R.M.; De Menezes, A.S.; Sinfrônio, F.S.M. Magnetic Ferrites Synthesised Using the Microwave-Hydrothermal Method. *J. Magn. Magn. Mater.* **2015**, *381*, 109–115. [CrossRef]

59. Beji, Z.; Ben Chaabane, T.; Smiri, L.S.; Ammar, S.; Fiévet, F.; Jouini, N.; Grenèche, J.M. Synthesis of Nickel–Zinc Ferrite Nanoparticles in Polyol: Morphological, Structural and Magnetic Studies. *Phys. Status Solidi* **2006**, *203*, 504–512. [CrossRef]

60. Ranjith Kumar, E.; Jayaprakash, R. The Role of Fuel Concentration on Particle Size and Dielectric Properties of Manganese Substituted Zinc Ferrite Nanoparticles. *J. Magn. Magn. Mater.* **2014**, *366*, 33–39. [CrossRef]

61. Aslibeiki, B.; Kameli, P.; Ehsani, M.H.; Salamati, H.; Muscas, G.; Agostinelli, E.; Foglietti, V.; Casciardi, S.; Peddis, D. Solvothermal Synthesis of MnFe2O4 Nanoparticles: The Role of Polymer Coating on Morphology and Magnetic Properties. *J. Magn. Magn. Mater.* **2016**, *399*, 236–244. [CrossRef]

62. Xie, J.; Yan, C.; Zhang, Y.; Gu, N. Shape Evolution of "Multibranched" Mn-Zn Ferrite Nanostructures with High Performance: A Transformation of Nanocrystals into Nanoclusters. *Chem. Mater.* **2013**, *25*, 3702–3709. [CrossRef]

63. Kumar, Y.; Sharma, A.; Shirage, P.M. Impact of Different Morphologies of CoFe2O4 Nanoparticles for Tuning of Structural, Optical and Magnetic Properties. *J. Alloys Compd.* **2019**, *778*, 398–409. [CrossRef]

64. Shan, A.; Wu, X.; Lu, J.; Chen, C.; Wang, R. Phase Formations and Magnetic Properties of Single Crystal Nickel Ferrite (NiFe2O4) with Different Morphologies. *CrystEngComm* **2015**, *17*, 1603–1608. [CrossRef]

65. Köseoğlu, Y.; Alan, F.; Tan, M.; Yilgin, R.; Öztürk, M. Low Temperature Hydrothermal Synthesis and Characterization of Mn Doped Cobalt Ferrite Nanoparticles. *Ceram. Int.* **2012**, *38*, 3625–3634. [CrossRef]

66. Wu, X.; Wang, W.; Song, N.; Yang, X.; Khaimanov, S.; Tsidaeva, N. From Nanosphere to Nanorod: Tuning Morphology, Structure and Performance of Cobalt Ferrites via Pr$^{3+}$ Doping. *Chem. Eng. J.* **2016**, *306*, 382–392. [CrossRef]

67. Rafienia, M.; Bigham, A.; Hassanzadeh-Tabrizi, S.A. Solvothermal Synthesis of Magnetic Spinel Ferrites. *J. Med. Signals Sens.* **2018**, *8*, 108. [CrossRef]

68. Hema, E.; Manikandan, A.; Karthika, P.; Antony, S.A.; Venkatraman, B.R. A Novel Synthesis of Zn$^{2+}$-Doped CoFe$_2$O$_4$ Spinel Nanoparticles: Structural, Morphological, Opto-Magnetic and Catalytic Properties. *J. Supercond. Nov. Magn.* **2015**, *28*, 2539–2552. [CrossRef]

69. Chen, J.; Wang, F.; Huang, K.; Liu, Y.; Liu, S. Preparation of Fe$_3$O$_4$ Nanoparticles with Adjustable Morphology. *J. Alloys Compd.* **2009**, *475*, 898–902. [CrossRef]

70. Zubair, A.; Ahmad, Z.; Mahmood, A.; Cheong, W.C.; Ali, I.; Khan, M.A.; Chughtai, A.H.; Ashiq, M.N. Structural, Morphological and Magnetic Properties of Eu-Doped CoFe$_2$O$_4$ Nano-Ferrites. *Results Phys.* **2017**, *7*, 3203–3208. [CrossRef]

71. Song, M.; Zhang, Y.; Hu, S.; Song, L.; Dong, J.; Chen, Z.; Gu, N. Influence of Morphology and Surface Exchange Reaction on Magnetic Properties of Monodisperse Magnetite Nanoparticles. *Colloids Surfaces A Physicochem. Eng. Asp.* **2012**, *408*, 114–121. [CrossRef]

72. Huang, Z.; Zhu, Y.; Zhang, J.; Yin, G. Stable Biomimetic Superhydrophobicity and Magnetization Film with Cu-Ferrite Nanorods. *J. Phys. Chem. C* **2007**, *111*, 6821–6825. [CrossRef]

73. Reitz, C.; Suchomski, C.; Chakravadhanula, V.S.K.; Djerdj, I.; Jagličić, Z.; Brezesinski, T. Morphology, Microstructure, and Magnetic Properties of Ordered Large-Pore Mesoporous Cadmium Ferrite Thin Film Spin Glasses. *Inorg. Chem.* **2013**, *52*, 3744–3754. [CrossRef]

74. Mohapatra, J.; Xing, M.; Beatty, J.; Elkins, J.; Seda, T.; Mishra, S.R.; Liu, J.P. Enhancing the Magnetic and Inductive Heating Properties of Fe$_3$O$_4$ Nanoparticles via Morphology Control. *Nanotechnology* **2020**, *31*, 275706. [CrossRef]

75. Sanchez-Lievanos, K.R.; Knowles, K.E. Controlling Cation Distribution and Morphology in Colloidal Zinc Ferrite Nanocrystals. *Chem. Mater.* **2022**, *34*, 7446–7459. [CrossRef]

76. Ansari, S.M.; Sinha, B.B.; Phase, D.; Sen, D.; Sastry, P.U.; Kolekar, Y.D.; Ramana, C.V. Particle Size, Morphology, and Chemical Composition Controlled CoFe$_2$O$_4$ Nanoparticles with Tunable Magnetic Properties via Oleic Acid Based Solvothermal Synthesis for Application in Electronic Devices. *ACS Appl. Nano Mater.* **2019**, *2*, 1828–1843. [CrossRef]

77. Goswami, P.P.; Choudhury, H.A.; Chakma, S.; Moholkar, V.S. Sonochemical Synthesis and Characterization of Manganese Ferrite Nanoparticles. *Ind. Eng. Chem. Res.* **2013**, *52*, 17848–17855. [CrossRef]

78. Zhang, Z.; Liu, Y.; Yao, G.; Zu, G.; Hao, Y. Synthesis and Characterization of NiFe$_2$O$_4$ Nanoparticles via Solid-State Reaction. *Int. J. Appl. Ceram. Technol.* **2013**, *10*, 142–149. [CrossRef]

79. Ranjithkumar, E.; Jayaprakash, R.; Kumar, S. Effect of Annealing Temperature on Structural and Magnetic Properties of Manganese Substituted NiFe$_2$O$_4$ Nanoparticles. *Mater. Sci. Semicond. Process.* **2014**, *17*, 173–177. [CrossRef]

80. Zhang, Z.; Liu, Y.; Yao, G.; Zu, G.; Zhang, X.; Ma, J. Solid-State Reaction Synthesis of NiFe$_2$O$_4$ Nanoparticles by Optimizing the Synthetic Conditions. *Phys. E Low-Dimens. Syst. Nanostruct.* **2012**, *45*, 122–129. [CrossRef]

81. Li, Y.; Gao, Y.; Fan, B.; Guan, L.; Zhao, B.; Zhang, R. Tailoring Microwave Electromagnetic Responses in Ti$_3$C$_2$Tx MXene with Fe$_3$O$_4$ Nanoparticle Decoration via a Solvothermal Method. *J. Phys. Chem. C* **2021**, *125*, 19914–19924. [CrossRef]

82. Shan, D.; He, J.; Deng, L.; Yan, S.; Luo, H.; Huang, S.; Xu, Y. The Underlying Mechanisms of Enhanced Microwave Absorption Performance for the NiFe$_2$O$_4$-Decorated Ti$_3$C$_2$Tx MXene. *Results Phys.* **2019**, *15*, 102750. [CrossRef]

83. Rasheed, T.; Rasheed, A.; Munir, S.; Ajmal, S.; Muhammad Shahzad, Z.; Alsafari, I.A.; Ragab, S.A.; Agboola, P.O.; Shakir, I. A Cost-Effective Approach to Synthesize NiFe$_2$O$_4$/MXene Heterostructures for Enhanced Photodegradation Performance and Anti-Bacterial Activity. *Adv. Powder Technol.* **2021**, *32*, 2248–2257. [CrossRef]

84. Qiu, F.; Wang, Z.; Liu, M.; Wang, Z.; Ding, S. Synthesis, Characterization and Microwave Absorption of MXene/NiFe$_2$O$_4$ Composites. *Ceram. Int.* **2021**, *47*, 24713–24720. [CrossRef]

85. Li, Y.; Zhou, X.; Wang, J.; Deng, Q.; Li, M.; Du, S.; Han, Y.H.; Lee, J.; Huang, Q. Facile Preparation of in Situ Coated Ti$_3$C$_2$Tx/Ni 0.5Zn0.5Fe$_2$O$_4$ Composites and Their Electromagnetic Performance. *RSC Adv.* **2017**, *7*, 24698–24708. [CrossRef]

86. He, J.; Liu, S.; Deng, L.; Shan, D.; Cao, C.; Luo, H.; Yan, S. Tunable Electromagnetic and Enhanced Microwave Absorption Properties in CoFe$_2$O$_4$ Decorated Ti$_3$C$_2$ MXene Composites. *Appl. Surf. Sci.* **2020**, *504*, 144210. [CrossRef]

87. Fayyaz, A.; Saravanakumar, K.; Talukdar, K.; Kim, Y.; Yoon, Y.; Park, C.M. Catalytic Oxidation of Naproxen in Cobalt Spinel Ferrite Decorated Ti$_3$C$_2$Tx MXene Activated Persulfate System: Mechanisms and Pathways. *Chem. Eng. J.* **2021**, *407*, 127842. [CrossRef]

88. Swapnalin, J.; Koneru, B.; Banerjee, P.; Natarajan, S.; Franco, A. Multilayer Intercalation: MXene/Cobalt Ferrite Electromagnetic Wave Absorbing Two-Dimensional Materials. *J. Phys. Chem. Solids* **2022**, *168*, 110797. [CrossRef]

89. Alsafari, I.A.; Munir, S.; Zulfiqar, S.; Saif, M.S.; Warsi, M.F.; Shahid, M. Synthesis, Characterization, Photocatalytic and Antibacterial Properties of Copper Ferrite/MXene (CuFe$_2$O$_4$/Ti$_3$C$_2$) Nanohybrids. *Ceram. Int.* **2021**, *47*, 28874–28883. [CrossRef]

90. Iqbal, M.A.; Ali, S.I.; Amin, F.; Tariq, A.; Iqbal, M.Z.; Rizwan, S. La-and Mn-Codoped Bismuth Ferrite/Ti$_3$C$_2$ MXene Composites for Efficient Photocatalytic Degradation of Congo Red Dye. *ACS Omega* **2019**, *4*, 8661–8668. [CrossRef]

91. Gao, Y.; Tang, Z.; Chen, X.; Yan, J.; Jiang, Y.; Xu, J.; Tao, Z.; Wang, L.; Liu, Z.; Wang, G. Magnetically Accelerated Thermal Energy Storage within Fe$_3$O$_4$-Anchored MXene-Based Phase Change Materials. *Aggregate* **2022**, *00*, e248. [CrossRef]

92. Arun, T.; Mohanty, A.; Rosenkranz, A.; Wang, B.; Yu, J.; Morel, M.J.; Udayabhaskar, R.; Hevia, S.A.; Akbari-Fakhrabadi, A.; Mangalaraja, R.V.; et al. Role of Electrolytes on the Electrochemical Characteristics of Fe3O4/MXene/RGO Composites for Supercapacitor Applications. *Electrochim. Acta* **2021**, *367*, 137473. [CrossRef]

93. Li, H.; Liu, Y.; Lin, S.; Li, H.; Wu, Z.; Zhu, L.; Li, C.; Wang, X.; Zhu, X.; Sun, Y. Laser Crystallized Sandwich-like MXene/Fe$_3$O$_4$/MXene Thin Film Electrodes for Flexible Supercapacitors. *J. Power Sources* **2021**, *497*, 229882. [CrossRef]

94. Guo, S.; Guan, H.; Li, Y.; Bao, Y.; Lei, D.; Zhao, T.; Zhong, B.; Li, Z. Dual-Loss Ti$_3$C$_2$Tx MXene/Ni$_{0.6}$Zn$_{0.4}$Fe$_2$O$_4$ Heterogeneous Nanocomposites for Highly Efficient Electromagnetic Wave Absorption. *J. Alloys Compd.* **2021**, *887*, 161298. [CrossRef]

95. Zhou, X.; Li, Y.; Huang, Q. Preparation of Ti3C2Tx/NiZn Ferrite Hybrids with Improved Electromagnetic Properties. *Materials* **2020**, *13*, 820. [CrossRef]

96. Lei, Y.; Yao, Z.; Li, S.; Zhou, J.; Haidry, A.A.; Liu, P. Broadband High-Performance Electromagnetic Wave Absorption of Co-Doped NiZn Ferrite/Polyaniline on MXenes. *Ceram. Int.* **2020**, *46*, 10006–10015. [CrossRef]

97. Wang, Z.; Cheng, Z.; Xie, L.; Hou, X.; Fang, C. Flexible and Lightweight Ti$_3$C$_2$Tx MXene/Fe$_3$O$_4$@PANI Composite Films for High-Performance Electromagnetic Interference Shielding. *Ceram. Int.* **2021**, *47*, 5747–5757. [CrossRef]

98. Wang, Y.; Gao, X.; Zhang, L.; Wu, X.; Wang, Q.; Luo, C.; Wu, G. Synthesis of Ti$_3$C$_2$/Fe$_3$O$_4$/PANI Hierarchical Architecture Composite as an Efficient Wide-Band Electromagnetic Absorber. *Appl. Surf. Sci.* **2019**, *480*, 830–838. [CrossRef]

99. Liu, G.; Xiong, Q.; Xu, Y.; Fang, Q.; Leung, K.C.F.; Sang, M.; Xuan, S.; Hao, L. Magnetically Separable MXene@Fe$_3$O$_4$/Au/PDA Nanosheets with Photothermal-Magnetolytic Coupling Antibacterial Performance. *Appl. Surf. Sci.* **2022**, *590*, 153125. [CrossRef]

100. Vikraman, D.; Hussain, S.; Hailiang, L.; Karuppasamy, K.; Sivakumar, P.; Santhoshkumar, P.; Jung, J.; Kim, H.-S. Spinel-Structured Metal Oxide-Embedded MXene Nanocomposites for Efficient Water Splitting Reactions. *Inorg. Chem. Front.* **2022**. [CrossRef]

101. Iqbal, M.A.; Tariq, A.; Zaheer, A.; Gul, S.; Ali, S.I.; Iqbal, M.Z.; Akinwande, D.; Rizwan, S. Ti3C2-MXene/Bismuth Ferrite Nanohybrids for Efficient Degradation of Organic Dyes and Colorless Pollutants. *ACS Omega* **2019**, *4*, 20530–20539. [CrossRef]

102. Deng, B.; Wang, L.; Xiang, Z.; Liu, Z.; Pan, F.; Lu, W. Rational Construction of MXene/Ferrite@C Hybrids with Improved Impedance Matching for High-Performance Electromagnetic Absorption Applications. *Mater. Lett.* **2021**, *284*, 129029. [CrossRef]

103. Yang, H.; Dai, J.; Liu, X.; Lin, Y.; Wang, J.; Wang, L.; Wang, F. Layered PVB/Ba$_3$Co$_2$Fe$_{24}$O$_{41}$/Ti$_3$C$_2$ Mxene Composite: Enhanced Electromagnetic Wave Absorption Properties with High Impedance Match in a Wide Frequency Range. *Mater. Chem. Phys.* **2017**, *200*, 179–186. [CrossRef]

104. Yu, L.; Luo, B.; Zhou, X.; Liu, Y.; Lan, F.; Wu, Y. In Situ Controllable Fabrication of Two-Dimensional Magnetic Fe$_3$O$_4$/TiO$_2$@Ti$_3$C$_2$Tx Composites for Highly Efficient Phosphopeptides Enrichment. *ACS Appl. Mater. Interfaces* **2021**, *13*, 54665–54676. [CrossRef]

105. Liu, H.; Wang, Z.; Yang, Y.; Wu, S.; Wang, C.; You, C.; Tian, N. Thermally Conductive MWCNTs/Fe$_3$O$_4$/Ti$_3$C$_2$Tx MXene Multi-Layer Films for Broadband Electromagnetic Interference Shielding. *J. Mater. Sci. Technol.* **2022**, *130*, 75–85. [CrossRef]

106. Cui, Y.; Yang, K.; Wang, J.; Shah, T.; Zhang, Q.; Zhang, B. Preparation of Pleated RGO/MXene/Fe$_3$O$_4$ Microsphere and Its Absorption Properties for Electromagnetic Wave. *Carbon N. Y.* **2021**, *172*, 1–14. [CrossRef]

107. Hu, Y.; Hou, C.; Shi, Y.; Wu, J.; Yang, D.; Huang, Z.; Wang, Y.; Liu, Y. Freestanding Fe3O4/Ti3C2TXMXene/Polyurethane Composite Film with Efficient Electromagnetic Shielding and Ultra-Stretchable Performance. *Nanotechnology* **2022**, *33*, 165603. [CrossRef]

108. Zhang, Y.; Ma, Z.; Ruan, K.; Gu, J. Multifunctional Ti$_3$C$_2$Tx-(Fe$_3$O$_4$/Polyimide) Composite Films with Janus Structure for Outstanding Electromagnetic Interference Shielding and Superior Visual Thermal Management. *Nano Res.* **2022**, *15*, 5601–5609. [CrossRef]

109. Cui, Y.; Liu, M.; Huang, H.; Zhang, D.; Chen, J.; Mao, L.; Zhou, N.; Deng, F.; Zhang, X.; Wei, Y. A Novel One-Step Strategy for Preparation of Fe$_3$O$_4$-Loaded Ti$_3$C$_2$ MXenes with High Efficiency for Removal Organic Dyes. *Ceram. Int.* **2020**, *46*, 11593–11601. [CrossRef]

110. Rethinasabapathy, M.; Bhaskaran, G.; Park, B.; Shin, J.Y.; Kim, W.S.; Ryu, J.; Huh, Y.S. Iron Oxide (Fe$_3$O$_4$)-Laden Titanium Carbide (Ti$_3$C$_2$Tx) MXene Stacks for the Efficient Sequestration of Cationic Dyes from Aqueous Solution. *Chemosphere* **2022**, *286*, 131679. [CrossRef]

111. Wang, Y.; Li, Y.; Qiu, Z.; Wu, X.; Zhou, P.; Zhou, T.; Zhao, J.; Miao, Z.; Zhou, J.; Zhuo, S. Fe$_3$O$_4$@Ti$_3$C$_2$ MXene Hybrids with Ultrahigh Volumetric Capacity as an Anode Material for Lithium-Ion Batteries. *J. Mater. Chem. A* **2018**, *6*, 11189–11197. [CrossRef]

112. Xu, D.; Ma, K.; Chen, L.; Hu, Y.; Jiang, H.; Li, C. MXene Interlayer Anchored Fe$_3$O$_4$ Nanocrystals for Ultrafast Li-Ion Batteries. *Chem. Eng. Sci.* **2020**, *212*, 115342. [CrossRef]

113. Jin, L.; Wang, J.; Wu, F.; Yin, Y.; Zhang, B. MXene@Fe$_3$O$_4$ Microspheres/Fibers Composite Microwave Absorbing Materials: Optimum Composition and Performance Evaluation. *Carbon N. Y.* **2021**, *182*, 770–780. [CrossRef]

114. Cui, Y.; Zhang, D.; Shen, K.; Nie, S.; Liu, M.; Huang, H.; Deng, F.; Zhou, N.; Zhang, X.; Wei, Y. Biomimetic Anchoring of Fe$_3$O$_4$ onto Ti$_3$C$_2$ MXene for Highly Efficient Removal of Organic Dyes by Fenton Reaction. *J. Environ. Chem. Eng.* **2020**, *8*, 104369. [CrossRef]

115. Liu, P.; Yao, Z.; Ng, V.M.H.; Zhou, J.; Kong, L.B.; Yue, K. Facile Synthesis of Ultrasmall Fe$_3$O$_4$ Nanoparticles on MXenes for High Microwave Absorption Performance. *Compos. Part A Appl. Sci. Manuf.* **2018**, *115*, 371–382. [CrossRef]

116. Zhang, P.; Sun, N.; Soomro, R.A.; Yue, S.; Zhu, Q.; Xu, B. Interface-Engineered Fe3O4/MXene Heterostructures for Enhanced Lithium-Ion Storage. *ACS Appl. Energy Mater.* **2021**, *4*, 11844–11853. [CrossRef]

117. Hu, Y.; Chu, H.; Ma, X.; Li, Y.; Zhao, S.; Li, D. Enhanced Optical Nonlinearities in Ti$_3$C$_2$ MXene Decorated Fe$_3$O$_4$ Nanocomposites for Highly Stable Ultrafast Pulse Generation. *Mater. Today Phys.* **2021**, *21*, 100482. [CrossRef]

118. Liu, P.; Ng, V.M.H.; Yao, Z.; Zhou, J.; Kong, L.B. Ultrasmall Fe$_3$O$_4$ Nanoparticles on MXenes with High Microwave Absorption Performance. *Mater. Lett.* **2018**, *229*, 286–289. [CrossRef]

119. Wang, X.; Chen, W.; Liao, Y.; Xiang, Q.; Li, Y.; Wen, T.; Zhong, Z. Accordion-like Composite of Carbon-Coated Fe$_3$O$_4$ Nanoparticle Decorated Ti$_3$C$_2$ MXene with Enhanced Electrochemical Performance. *J. Mater. Sci.* **2021**, *56*, 2486–2496. [CrossRef]

120. Zhang, X.; Wang, H.; Hu, R.; Huang, C.; Zhong, W.; Pan, L.; Feng, Y.; Qiu, T.; Zhang, C.; Yang, J. Novel Solvothermal Preparation and Enhanced Microwave Absorption Properties of Ti$_3$C$_2$Tx MXene Modified by in Situ Coated Fe$_3$O$_4$ Nanoparticles. *Appl. Surf. Sci.* **2019**, *484*, 383–391. [CrossRef]

121. Xu, J.; Tang, S.; Liu, D.; Bai, Z.; Xie, X.; Tian, X.; Xu, W.; Hou, W.; Meng, X.; Yang, N. Rational Design of Hollow Fe$_3$O$_4$ Microspheres on Ti$_3$C$_2$Tx MXene Nanosheets as Highly-Efficient and Lightweight Electromagnetic Absorbers. *Ceram. Int.* **2022**, *48*, 2595–2604. [CrossRef]

122. Kong, F.; He, X.; Liu, Q.; Qi, X.; Sun, D.; Zheng, Y.; Wang, R.; Bai, Y. Further Surface Modification by Carbon Coating for In-Situ Growth of Fe$_3$O$_4$ Nanoparticles on MXene Ti$_3$C$_2$ Multilayers for Advanced Li-Ion Storage. *Electrochim. Acta* **2018**, *289*, 228–237. [CrossRef]

123. Li, Q.; Zhou, J.; Li, F.; Sun, Z. Spring-Roll-like Ti$_3$C$_2$ MXene/Carbon-Coated Fe3O4 Composite as a Long-Life Li-Ion Storage Material. *Inorg. Chem. Front.* **2020**, *7*, 3491–3499. [CrossRef]

124. Wang, Y.; Qi, Q.; Yin, G.; Wang, W.; Yu, D. Flexible, Ultralight, and Mechanically Robust Waterborne Polyurethane/Ti$_3$C$_2$T XMXene/Nickel Ferrite Hybrid Aerogels for High-Performance Electromagnetic Interference Shielding. *ACS Appl. Mater. Interfaces* **2021**, *13*, 21831–21843. [CrossRef]

125. Guo, Y.; Zhang, D.; Yang, Y.; Wang, Y.; Bai, Z.; Chu, P.K.; Luo, Y. MXene-Encapsulated Hollow Fe$_3$O$_4$ Nanochains Embedded in N-Doped Carbon Nanofibers with Dual Electronic Pathways as Flexible Anodes for High-Performance Li-Ion Batteries. *Nanoscale* **2021**, *13*, 4624–4633. [CrossRef]

126. Hu, Y.; Hou, C.; Du, J.; Fan, Q.; Fang, J.; Shi, Y.; Yang, G.; An, J.; Liu, Y. Flexible Sensor Based on Fe$_3$O$_4$-COOH@Ti$_3$C$_2$Tx MXene Rapid-Gelating Hydrogel for Human Motion Monitoring. *Adv. Mater. Interfaces* **2022**, *9*, 2200487. [CrossRef]

127. Song, Q.; Chen, B.; Zhou, Z.; Lu, C. Flexible, Stretchable and Magnetic Fe$_3$O$_4$@Ti$_3$C$_2$Tx/Elastomer with Supramolecular Interfacial Crosslinking for Enhancing Mechanical and Electromagnetic Interference Shielding Performance. *Sci. China Mater.* **2021**, *64*, 1437–1448. [CrossRef]

128. Tahir, K.; Miran, W.; Jang, J.; Maile, N.; Shahzad, A.; Moztahida, M.; Ghani, A.A.; Kim, B.; Jeon, H.; Lim, S.R.; et al. Nickel Ferrite/MXene-Coated Carbon Felt Anodes for Enhanced Microbial Fuel Cell Performance. *Chemosphere* **2021**, *268*, 128784. [CrossRef]

129. Liu, T.; Zhang, N.; Zhang, K.; Wang, Y.; Qi, Y.; Zong, M. Multi-Components Matching Manipulation of MXene/PPy@β2-SiW11Co/Fe$_3$O$_4$ Nanocomposites for Enhancing Electromagnetic Wave Absorption Performance. *Compos. Part A Appl. Sci. Manuf.* **2022**, *159*, 107020. [CrossRef]

130. Liang, W.; Zhitomirsky, I. Composite Fe3O4-MXene-Carbon Nanotube Electrodes for Supercapacitors Prepared Using the New Colloidal Method. *Materials* **2021**, *14*, 2930. [CrossRef]

131. Cui, C.; Guo, R.; Ren, E.; Xiao, H.; Zhou, M.; Lai, X.; Qin, Q.; Jiang, S.; Qin, W. MXene-Based RGO/Nb$_2$CTx/Fe$_3$O$_4$ Composite for High Absorption of Electromagnetic Wave. *Chem. Eng. J.* **2021**, *405*, 126626. [CrossRef]

132. Bund, A.; Koehler, S.; Kuehnlein, H.H.; Plieth, W. Magnetic Field Effects in Electrochemical Reactions. *Electrochim. Acta* **2003**, *49*, 147–152. [CrossRef]

133. O'Brien, R.N.; Santhanam, K.S.V. Magnetic Field Assisted Convection in an Electrolyte of Nonuniform Magnetic Susceptibility. *J. Appl. Electrochem.* **1997**, *27*, 573–578. [CrossRef]

134. Monzon, L.M.A.; Coey, J.M.D. Magnetic Fields in Electrochemistry: The Lorentz Force. A Mini-Review. *Electrochem. commun.* **2014**, *42*, 38–41. [CrossRef]

135. Huang, Y.; Huang, Y.; Zhu, M.; Meng, W.; Pei, Z.; Liu, C.; Hu, H.; Zhi, C. Magnetic-Assisted, Self-Healable, Yarn-Based Supercapacitor. *ACS Nano* **2015**, *9*, 6242–6251. [CrossRef]

136. Innocenti, M.; Passaponti, M.; Giurlani, W.; Giacomino, A.; Pasquali, L.; Giovanardi, R.; Fontanesi, C. Spin Dependent Electrochemistry: Focus on Chiral vs Achiral Charge Transmission through 2D SAMs Adsorbed on Gold. *J. Electroanal. Chem.* **2020**, *856*, 113705. [CrossRef]

137. Roy, K.; Devi, P.; Kumar, P. Magnetic-Field Induced Sustainable Electrochemical Energy Harvesting and Storage Devices: Recent Progress, Opportunities, and Future Perspectives. *Nano Energy* **2021**, *87*, 106119. [CrossRef]

138. Fahidy, T.Z. Magnetoelectrolysis. *J. Appl. Electrochem.* **1983**, *13*, 553–563. [CrossRef]

139. Zhang, W.; Gao, W.; Zhang, X.; Li, Z.; Lu, G. Surface Spintronics Enhanced Photo-Catalytic Hydrogen Evolution: Mechanisms, Strategies, Challenges and Future. *Appl. Surf. Sci.* **2018**, *434*, 643–668. [CrossRef]

140. Okumura, H.; Endo, S.; Joonwichien, S.; Yamasue, E.; Ishihara, K.N. Magnetic Field Effect on Heterogeneous Photocatalysis. *Catal. Today* **2015**, *258*, 634–647. [CrossRef]

141. Gatard, V.; Deseure, J.; Chatenet, M. Use of Magnetic Fields in Electrochemistry: A Selected Review. *Curr. Opin. Electrochem.* **2020**, *23*, 96–105. [CrossRef]

142. Açıkkalp, E.; Altuntas, O.; Caliskan, H.; Grisolia, G.; Lucia, U.; Borge-Diez, D.; Rosales-Asensio, E. Sustainability Analyses of Photovoltaic Electrolysis and Magnetic Heat Engine Coupled Novel System Used for Hydrogen Production and Electricity Generation. *Sustain. Energy Technol. Assess.* **2022**, *52*, 102094. [CrossRef]

143. Zhang, L.; Zeng, Z.; Wang, D.W.; Zuo, Y.; Chen, J.; Yan, X. Magnetic Field-Induced Capacitance Change in Aqueous Carbon-Based Supercapacitors. *Cell Reports Phys. Sci.* **2021**, *2*, 100455. [CrossRef]

144. Pal, S.; Majumder, S.; Dutta, S.; Banerjee, S.; Satpati, B.; De, S. Magnetic Field Induced Electrochemical Performance Enhancement in Reduced Graphene Oxide Anchored $Fe_3O_4$ Nanoparticle Hybrid Based Supercapacitor. *J. Phys. D. Appl. Phys.* **2018**, *51*, 375501. [CrossRef]

145. Zhu, J.; Chen, M.; Qu, H.; Luo, Z.; Wu, S.; Colorado, H.A.; Wei, S.; Guo, Z. Magnetic Field Induced Capacitance Enhancement in Graphene and Magnetic Graphene Nanocomposites. *Energy Environ. Sci.* **2013**, *6*, 194–204. [CrossRef]

146. Singh, M.; Sahoo, A.; Yadav, K.L.; Sharma, Y. Toward the Origin of Magnetic Field-Dependent Storage Properties: A Case Study on the Supercapacitive Performance of $FeCo_2O_4$ Nanofibers. *ACS Appl. Mater. Interfaces* **2020**, *12*, 49530–49540. [CrossRef] [PubMed]

147. Wang, G.; Xu, H.; Lu, L.; Zhao, H. Magnetization-Induced Double-Layer Capacitance Enhancement in Active Carbon/$Fe_3O_4$ Nanocomposites. *J. Energy Chem.* **2014**, *23*, 809–815. [CrossRef]

148. Wei, H.; Gu, H.; Guo, J.; Cui, D.; Yan, X.; Liu, J.; Cao, D.; Wang, X.; Wei, S.; Guo, Z. Significantly Enhanced Energy Density of Magnetite/Polypyrrole Nanocomposite Capacitors at High Rates by Low Magnetic Fields. *Adv. Compos. Hybrid Mater.* **2017**, *1*, 127–134. [CrossRef]

149. Haldar, P.; Biswas, S.; Sharma, V.; Chandra, A. Understanding the Origin of Magnetic Field Dependent Specific Capacitance in $Mn_3O_4$ Nanoparticle Based Supercapacitors. *J. Electrochem. Soc.* **2018**, *165*, A3230–A3239. [CrossRef]

150. Zhang, H.; Han, Z.; Deng, Q. The Effect of an External Magnetic Field on the Electrochemical Capacitance of Nanoporous Nickel for Energy Storage. *Nanomaterials* **2019**, *9*, 694. [CrossRef]

151. Singh, M.; Sahoo, A.; Yadav, K.L.; Sharma, Y. Role of Magnetism Present in the Cobaltites ($ACo_2O_4$ A = Co, Mn, and Fe) on the Charge Storage Mechanism in Aqueous Supercapacitor. *Appl. Surf. Sci.* **2021**, *568*, 150966. [CrossRef]

152. Zhu, J.; Chen, M.; Wei, H.; Yerra, N.; Haldolaarachchige, N.; Luo, Z.; Young, D.P.; Ho, T.C.; Wei, S.; Guo, Z. Magnetocapacitance in Magnetic Microtubular Carbon Nanocomposites under External Magnetic Field. *Nano Energy* **2014**, *6*, 180–192. [CrossRef]

153. Sharma, V.; Biswas, S.; Chandra, A. Need for Revisiting the Use of Magnetic Oxides as Electrode Materials in Supercapacitors: Unequivocal Evidence of Significant Variation in Specific Capacitance under Variable Magnetic Field. *Adv. Energy Mater.* **2018**, *8*, 1800573. [CrossRef]

154. Devi, P.; Srivastava, M.; Kim, N.H.; Lee, J.H.; Mishra, D. Efficient Energy Storage Performance of in Situ Grown $Co_3V_2O_8$-RGO Composite Nanostructure for High Performance Asymmetric $Co_3V_2O_8$-RGO//RGO Supercapacitors and Consequence of Magnetic Field Induced Enhanced Capacity. *Compos. Part B Eng.* **2021**, *227*, 109384. [CrossRef]

155. Keyang, H.; Ruiyi, L.; Zaijun, L.; Yongqiang, Y. Controllable Synthesis of Superparamagnetic NiCo-Graphene Quantum Dot-Graphene Composite with Excellent Dispersion for High Performance Magnetic Field-Controlled Electrochemical Flow Hybrid Supercapacitor. *Electrochim. Acta* **2020**, *353*, 136524. [CrossRef]

156. Zeng, Z.; Liu, Y.; Zhang, W.; Chevva, H.; Wei, J. Improved Supercapacitor Performance of $MnO_2$-Electrospun Carbon Nanofibers Electrodes by MT Magnetic Field. *J. Power Sources* **2017**, *358*, 22–28. [CrossRef]

157. Ganguly, D.; Ajay, A.P.; Ghosh, A.; Ramaprabhu, S. Magnetic Field Assisted High Capacity Durable Li-Ion Battery Using Magnetic $\alpha$-$Fe_2O_3$ Nanoparticles Decorated Expired Drug Derived N-Doped Carbon Anode. *Sci. Rep.* **2020**, *10*, 9945. [CrossRef]

158. Szczesí, A.; Chibowski, E.; Hołysz, L.; Rafalski, P. Effects of Static Magnetic Field on Electrolyte Solutions under Kinetic Condition. *J. Phys. Chem. A* **2011**, *115*, 5449–5452. [CrossRef]

159. Sueptitz, R.; Koza, J.; Uhlemann, M.; Gebert, A.; Schultz, L. Magnetic Field Effect on the Anodic Behaviour of a Ferromagnetic Electrode in Acidic Solutions. *Electrochim. Acta* **2009**, *54*, 2229–2233. [CrossRef]

160. Oshitani, J.; Yamada, D.; Miyahara, M.; Higashitani, K. Magnetic Effect on Ion-Exchange Kinetics. *J. Colloid Interface Sci.* **1999**, *210*, 1–7. [CrossRef]
161. Shi, L.; Wang, X.; Hu, Y.; He, Y. Investigation of Photocatalytic Activity through Photo-Thermal Heating Enabled by Fe3O4/TiO2 Composite under Magnetic Field. *Sol. Energy* **2020**, *196*, 505–512. [CrossRef]
162. Peng, C.; Fan, W.; Li, Q.; Han, W.; Chen, X.; Zhang, G.; Yan, Y.; Gu, Q.; Wang, C.; Zhang, H.; et al. Boosting Photocatalytic Activity through Tuning Electron Spin States and External Magnetic Fields. *J. Mater. Sci. Technol.* **2022**, *115*, 208–220. [CrossRef]
163. Zhao, C.; Zhou, L.; Zhang, Z.; Gao, Z.; Weng, H.; Zhang, W.; Li, L.; Song, Y.Y. Insight of the Influence of Magnetic-Field Direction on Magneto-Plasmonic Interfaces for Tuning Photocatalytical Performance of Semiconductors. *J. Phys. Chem. Lett.* **2020**, *11*, 9931–9937. [CrossRef]
164. Gao, W.; Liu, Q.; Zhang, S.; Yang, Y.; Zhang, X.; Zhao, H.; Qin, W.; Zhou, W.; Wang, X.; Liu, H.; et al. Electromagnetic Induction Derived Micro-Electric Potential in Metal-Semiconductor Core-Shell Hybrid Nanostructure Enhancing Charge Separation for High Performance Photocatalysis. *Nano Energy* **2020**, *71*, 104624. [CrossRef]
165. Bian, Y.; Zheng, G.; Ding, W.; Hu, L.; Sheng, Z. Magnetic Field Effect on the Photocatalytic Degradation of Methyl Orange by Commercial TiO2 Powder. *RSC Adv.* **2021**, *11*, 6284–6291. [CrossRef] [PubMed]
166. Gao, L.; Wang, C.; Li, R.; Li, R.; Chen, Q. The Effect of External Magnetic Fields on the Catalytic Activity of Pd Nanoparticles in Suzuki Cross-Coupling Reactions. *Nanoscale* **2016**, *8*, 8355–8362. [CrossRef] [PubMed]
167. Fahidy, T.Z. Hydrodynamic Models in Magnetoelectrolysis. *Electrochim. Acta* **1973**, *18*, 607–614. [CrossRef]
168. Garcés-Pineda, F.A.; Blasco-Ahicart, M.; Nieto-Castro, D.; López, N.; Galán-Mascarós, J.R. Direct Magnetic Enhancement of Electrocatalytic Water Oxidation in Alkaline Media. *Nat. Energy* **2019**, *4*, 519–525. [CrossRef]
169. Rurainsky, C.; Nettler, D.-R.; Pahl, T.; Just, A.; Cignoni, P.; Kanokkanchana, K.; Tschulik, K. Electrochemical Dealloying in a Magnetic Field—Tapping the Potential for Catalyst and Material Design. *Electrochim. Acta* **2022**, *426*, 140807. [CrossRef]
170. Lu, Y.; Zhu, T.; Zhang, G.; He, Z.; Lin, C.; Chen, Y.; Guo, H. Influence of Magnetic Fields on the Morphology and Pseudocapacitive Properties of NiO on Nickel Foam. *RSC Adv.* **2015**, *5*, 99745–99753. [CrossRef]
171. Matsushima, H.; Bund, A.; Plieth, W.; Kikuchi, S.; Fukunaka, Y. Copper Electrodeposition in a Magnetic Field. *Electrochim. Acta* **2007**, *53*, 161–166. [CrossRef]
172. Aaboubi, O.; Douglade, J. Application of Magnetic Field to Control Mass Transport Process during Silver Cementation on Copper. *J. Electroanal. Chem.* **2013**, *693*, 42–50. [CrossRef]
173. Ganesh, V.; Vijayaraghavan, D.; Lakshminarayanan, V. Fine Grain Growth of Nickel Electrodeposit: Effect of Applied Magnetic Field during Deposition. *Appl. Surf. Sci.* **2005**, *240*, 286–295. [CrossRef]
174. Matsushima, H.; Ispas, A.; Bund, A.; Plieth, W.; Fukunaka, Y. Magnetic Field Effects on Microstructural Variation of Electrodeposited Cobalt Films. *J. Solid State Electrochem.* **2007**, *11*, 737–743. [CrossRef]
175. Ispas, A.; Matsushima, H.; Plieth, W.; Bund, A. Influence of a Magnetic Field on the Electrodeposition of Nickel–Iron Alloys. *Electrochim. Acta* **2007**, *52*, 2785–2795. [CrossRef]
176. Dai, P.; Yan, T.; Hu, L.; Pang, Z.; Bao, Z.; Wu, M.; Li, G.; Fang, J.; Peng, Z. Phase Engineering of Cobalt Hydroxides Using Magnetic Fields for Enhanced Supercapacitor Performance. *J. Mater. Chem. A* **2017**, *5*, 19203–19209. [CrossRef]